MNRAS 000, 1–25 (2021) Preprint 28 March 2022 Compiled using MNRAS LATEX style file v3.0

Double flows anchored in a Kerr black hole horizon. I. Meridionally self-similar MHD models with loading terms

L. Chantry[1]★, V. Cayatte[1], C. Sauty[1,2], N. Vlahakis[3], K. Tsinganos[3]
[1]*Laboratoire Univers et Théories, Observatoire de Paris - PSL, UMR 8102 du CNRS, Université Paris Diderot, F-92190 Meudon, France*
[2]*Laboratoire Univers et Particules de Montpellier (LUPM) Université Montpellier, CNRS/IN2P3, CC72, place Eugéne Bataillon, 34095, Montpellier Cedex 5, France*
[3]*Section of Astrophysics, Astronomy and Mechanics, Department of Physics, University of Athens, Panepistimiopolis Zografos, Athens 15783, Greece*

Submitted 31/03/2022

ABSTRACT

Recent observations of supermassive black holes have brought us new information on black hole magnetospheres. This may help us to understand the mechanisms involved in such magnetospheres, especially the origin of the observed powerful jets. In the double beam paradigm, pairs can be created in the black hole magnetosphere filling the polar axis region. In these models, some pairs are falling onto the black hole in the form of an inflow, while the remaining pairs are outflowing in the form of a spine jet. Our purpose in this paper is to build a complete and consistent description of this inflow-outflow structure. By knowing the MHD field on the black hole horizon allows us to properly calculate the amount of extracted angular momentum and energy from the black hole. In this way we get a consistent method to calculate the energy flux decomposition into Penrose and Blandford-Znajek processes on the horizon. We assume ideal, steady and axisymmetric MHD fluids. Both the outflow and the inflow structures, where there is no injection of pairs are described near the axis by meridional self-similar MHD models. We match the inflow and the outflow solutions of these models in order to get the required double flow structure. The matching of these two flows requires the creation of pairs on the stagnation layer, which separates the two flows. We present three solutions by showing three different types of energetic interaction between the MHD fields and the black hole. In all solutions, angular momentum and Poynting flux are extracted from the black hole. Globally, in all three solutions more energy is absorbed than extracted from the black hole. In the first one, the energy exchange with the black hole is dominated by the mass, thermal and kinetic energies of the flow and consequently there is no extraction of energy. In the second solution, the Penrose process dominates at large colatitudes. The third solution is Poynting flux dominated at mid colatitudes. The magnetic field is fitted to the values obtained from the observation of the black hole silouette in M87. For the two last solutions the mass injection rate is on the upper limit of the estimation range that is obtained via pair creation from the hard photons coming from the accretion disk. The Poynting power of these solutions is mainly due to the power brought in by the pair injection. In the last inflow solution, the isorotation pulsation is equal to one half of the black hole one and the extracted Poynting flux from the black hole comparable to the one obtained by the free force assumption. Our inflow/outflow solutions are promising to describe the plasma flow along the polar axis where gap formation could be prevented. They furnish an outflow with a power expected for extragalactic jets.

Key words: Black hole physics – Magnetohydrodynamics (MHD) –Relativistic processes – Galaxies: jets

INTRODUCTION

The recent images taken by the Event Horizon Telescope of the M87 black hole have brought us new information on the black hole magnetosphere, such as the estimation of the diameter of its photon ring, or the value of its surrounding magnetic field (Event Horizon Telescope Collaboration 2019, 2021). This can help us to understand the mechanisms involved in such magnetospheres, especially the origin of their observed powerful jets.

Despite recent progress on the magnetohydrodynamics (MHD) of rotating black holes (e.g. Yao et al. (2021), Huang et al. (2019), Pu & Takahashi (2020)), several properties of their plasma-filled magnetospheres are not completely known. In particular, the energy release at the base of jets from Active Galactic Nuclei (AGN) and Gamma Ray Bursts (GRB) may be explained via several mechanisms, depending on the geometry and the physical content of the black hole magnetosphere. The extraction of rotational energy from spinning black holes started to be theoretically investigated already in the 1970's (Penrose & Floyd 1971) and continued afterwards.

A necessary condition for an extraction mechanism to take place is the existence of an ergo-region in the immediate vicinity of the black hole horizon. In the case where the black hole is pervaded with a magnetic field, this extraction may take place in two different ways. The extraction occurs either via the plasma itself or via the electromagnetic field. If the plasma inertia dominates, we have the so-called generalised Penrose mechanism. If the Poynting flux dominates, we have the so-called generalised Blandford-Znajek mechanism. Strictly

★ E-mail: loic.chantry@obspm.fr

speaking, the Blandford-Znajek mechanism applies in a force free magnetosphere.

Penrose (1969) was the first to propose a mechanical process for extracting black hole energy, using the splitting of particles in the ergosphere. This process happens if one of the particle resulting from the splitting falls onto the black hole with negative energy and the other one reaches infinity with more energy than the entering particle.

On the other hand, neglecting the plasma inertia, Blandford & Znajek (1977) proposed a stationary model for energy extraction via the Poynting flux of the bulk electromagnetic field threading the black hole. In this model, where the fluid energy flux is negligible, they developed a perturbation method for the force-free equations of electrodynamics as a function of the black hole spin parameter. Then, they applied this analytical description to a split monopole configuration modelling a black hole surrounded by an accretion disc. Thus they showed that, for a given black hole angular momentum variation, the energy extracted from the black hole can reach 50% of the maximum extractable energy.

These two fundamental mechanisms and their application to astrophysical phenomena are still discussed for different reasons. For example, causality agreement in the extraction of black hole rotational energy has been clearly established only for the Penrose process. The Blandford-Znajek mechanism does not explained how the electromagnetic Poynting flux is causally produced and how the black hole rotational energy is reduced (Punsly & Coroniti 1990, Komissarov 2009, Koide & Baba 2014, Toma & Takahara 2016).

The expected very low rate of particle production with a relative velocity between the two fragments larger than $c/2$, seems to produce a very inefficient Penrose process (Bardeen et al. 1972, Wald 1974). Yet, Wagh et al. (1985) showed that the electromagnetic field may provide the required energy to put one fragment onto a negative energy orbit, without any constraint on its relative velocity (for a review of the mechanical Penrose-type processes see Wagh & Dadhich 1989). Then, a magnetic Penrose process could be extremely efficient in the entire range of expected magnetic fields (Dadhich et al. 2018). The plasma within the ergo-region plays the role of negative energy particles in the rotational energy extraction from the black hole. Time-dependent numerical simulations tend to support that the energy is supplied into jets from the rotational energy of the black hole (Koide et al. 2002, Komissarov 2004, Komissarov & McKinney 2007, McKinney et al. 2012). However, simulations (e.g., Komissarov (2005) and McKinney (2006)) show that the Penrose process seems to be a transient phenomenon, which is lately replaced by a pure electromagnetic mechanism similar to the original Blandford-Znajek one.

In this study, we consider AGN jets, produced in the immediate environment of rotating supermassive black holes. Jets are multi-component outflows. Most present models are based on having a faster, mainly leptonic, core flow (the spine jet) surrounded by an outer hadronic component with mildly relativistic speeds (the sheath layer or disk wind). This two stream model was firstly proposed by Sol et al. (1989) and allowed to get a unification scheme for BL Lac and radiogalaxy sources emission (Ghisellini et al. 2005). The disk wind component (proton-electron) can be modelled by radially self-similar models including the effects of magnetic fields, gravity and enthalpy (Vlahakis & Königl (2003), Ceccobello et al. (2018)). For the inner spine jet, we proposed in Chantry et al. (2018) an extension, in Kerr metric, of meridionally self-similar models (Sauty & Tsinganos 1994, Meliani et al. 2006, Globus et al. 2014). This non-force free model is adapted to describe the spine jet close to its polar axis. The Chantry et al. (2018) model was built without neglecting the light cylinder radius and allowed to define a magnetic collimation criterion.

In steady, axisymmetric and ideal MHD, the mass flux is a conserved quantity along the magnetic flux tubes. Material slides along magnetic flux tubes. Thus to have a jet one needs to have mass injection within the flow. Since, sufficiently close to the system axis, magnetic flux tubes are necessarily anchored onto the black hole horizon. Therefore, the only way to obtain an outflow on such tubes is to inject, at some location above the horizon. The main process capable of mass loading is the creation of electron/positron pairs. Levinson & Rieger (2011) estimate the amount of pairs produced from the hard photons emitted by a radiatively inefficient accretion disk. The authors conclude that the disk could not produce enough pairs to obtain the necessary Goldreich-Julian charge density in the black hole magnetosphere (Hirotani & Pu 2016 and references therein). Additionally, because of this low charge density, an electric gap forms, accelerating the particles along the flow. Due to an inverse Compton mechanism, the acceleration goes together with an increase of hard photon production. This induces the creation of additional pairs. These gap models have been studied extensively in the literature (Beskin et al. 1992; Hirotani & Okamoto 1998; Hirotani et al. 2016; Hirotani & Pu 2016; Levinson & Segev 2017). In particle-in-cell simulations (Crinquand et al. 2021), the magnetic reconnection on the equatorial plane and the formation of an intermittent spark gap lead to bursts of pair creation near the inner light cylinder. During these bursts, the density of pairs can reach values more than a thousand times the Goldreich-Julian density.

Camenzind (1986), Takahashi et al. (1990), and Hirotani et al. (1992) developed a general formalism allowing to solve the longitudinal fluid motion in a Kerr metric for a steady, axisymmetric, and magnetised flow in ideal MHD. This method requires that the geometry of the poloidal field lines is given, in order to solve the Bernoulli equation along the poloidal magnetic lines. Another way to deduce the field line shape is to solve the transverse Grad-Shafranov equation (see. Nitta et al. 1991, Beskin & Par'ev 1993 and Gourgoulhon et al. 2011). For a fixed geometry of the magnetic field lines, several approaches have been used to match the inflow and outflow solutions with loading terms localised on the stagnation surface (Globus & Levinson 2013, Pu et al. 2015, Pu & Takahashi 2020). For example, Huang et al. (2019) pursue this inflow/outflow matching approach by using the numerical methods introduced by Nathanail & Contopoulos (2014) to solve the Grad-Shafranov equation in the force-free approximation. Globus & Levinson (2014) used the Camenzind (1986) formalism with loading terms, controlling the magnitude of the bulk mass flux. In this paper, we present inflow/outflow solutions, continuing the meridionally self-similar model developed in Chantry et al. (2018), wherein we did not have loading terms. Additionally, this model can produce inflow solutions by reversing the flow direction.

The loading of matter occurs in a thin layer at the stagnation surface separating the inflow from the outflow. We solve the MHD equations for the inflow and outflow parts, satisfying the matching conditions at the stagnation surface in (see Sec.2).

This allows us to correctly quantify the energy and angular momentum exchanges between the rotating black hole and the magnetised flow surrounding it, without assuming force-free conditions. Hence, we may deduce from this model the mass, angular momentum and energy injected at the stagnation surface.

In Sec. 1, we derive the MHD equations for an ideal plasma in a Kerr metric under the assumptions of axisymmetry and steadiness. Furthermore, the 3+1 formalism is used with a mass loading term. In Sec. 2, we present the adopted model by assuming an injection layer and discussing the matching conditions that follow. In Sec. 3

we analyse three inflow/outflow solutions. In particular, we discuss the role of the magnitude of the mass injection rate, the kinetic and dynamical behaviour of the flows, as well as the interaction between the black hole and the MHD fields.

1 INFLOW AND OUTFLOW VIA PAIR INJECTION

We model the problem under the assumptions of stationarity and axisymmetry. This means that all physical quantities in our study are invariant with time and along the azimuthal coordinate. We also consider an ideal relativistic plasma in which takes place pair creation.

1.1 General Relativistic MHD Equations

The extraction of rotational energy from a central supermassive black hole is a mechanism suspected to play a dominant role in the formation of flows around it. Those energy extraction mechanisms are not limited *a priori* to the Penrose, or the Blandford-Znajek processes. One can generalise the problem of energy extraction by studying directly the Noether currents associated to the energy and angular momentum, see Lasota et al. (2014). In any case, the simplest space-time for this study is the Kerr space-time. It allows one to study those interactions between the black hole and the surrounding hydromagnetic field.

Choosing a Kerr space-time implies that we neglect the self-gravitation of the energy-momentum tensor field (plasma + radiation + electromagnetic fields). It is a reasonable assumption, because a perturbation to the Kerr metric due to the self-gravitation of the energy-momentum field is negligible compared to Kerr metric.

We call spine jet the outflow around the rotation axis launched from the vicinity of the black hole magnetosphere. The source of the spine jet energy could be the injection of matter/energy (pair creation, flow of energy in the magnetosphere or, any other mechanism), or the extraction of rotational energy from the black hole.

We construct a semi-analytical magnetohydrodynamic model (MHD) based on the self-similar technique, in a general relativistic frame. This model has already been presented in Chantry et al. (2018) and is an extension in a Kerr metric of a similar model developed in a Schwarzschild metric (Meliani et al. 2006). Here we present the combination of outflow and inflow solutions in order to describe the jet from the black hole up to large distances. The outflow starts at some stagnation radius to reach a large distance and the inflow starts also at the same stagnation radius to fall into the black hole horizon (Fig. 1).

Let $(\mathcal{M};\mathbf{g})$ be the Kerr manifold using the usual Boyer-Lindquist map coordinates. Its line element is,

$$\mathrm{ds}^2 = -\frac{\rho^2\Delta}{\Sigma^2}\mathrm{c}^2\mathrm{dt}^2 + \varpi^2\left(\mathrm{d}\varphi - \frac{\omega}{\mathrm{c}}\mathrm{cdt}\right)^2 + \frac{\rho^2}{\Delta}\mathrm{dr}^2 + \rho^2\mathrm{d}\theta^2\,, \tag{1}$$

where,

$$\Delta = r^2 + r_g^2a^2 - 2r_gr\,, \quad \rho^2 = r^2 + r_g^2a^2\cos^2\theta\,,$$
$$\varpi = \frac{\Sigma}{\rho}\sin\theta\,, \qquad \omega = \frac{2r_g^2acr}{\Sigma^2}\,,$$

$$\Sigma^2 = (r^2 + r_g^2a^2)^2 - r_g^2a^2\Delta\sin^2\theta\,,$$

with

$$a = \frac{\mathcal{J}c}{\mathrm{M}^2\mathcal{G}}\,, \qquad r_g = \frac{\mathcal{G}\mathrm{M}}{c^2}\,,$$

the dimensionless black hole spin ($0 \le a < 1$) and the gravitational radius, respectively. We note that $\mathcal{J}$ is the angular momentum of the massive central object and M its mass. Also note that ϖ corresponds to the usual Boyer-Lindquist cylindrical coordinate, i.e. $2\pi\varpi$ is the perimeter of the circle centered on the axis at constant t, θ, and r.

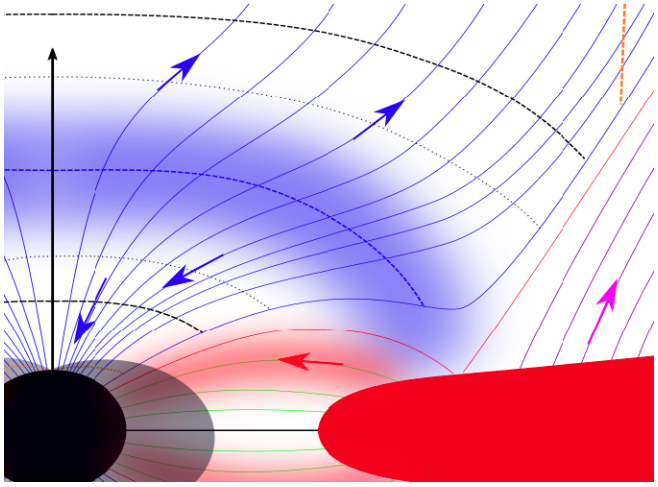

Figure 1. Schematic representation of the inflow/outflow configuration in the poloidal plane. The black surface corresponds to the black hole horizon and the light grey shaded region to the ergo-region. The blue lines and arrows correspond to the magnetic field lines anchored on the black hole horizon and reaching infinity. The green lines correspond to those lines of the black hole magnetosphere which link the disk to the black hole. The magenta lines and arrow corresponds to the magnetic field line anchored in the disk and reaching infinity. The blurred blue zone corresponds to the region where we expect that pair creation is efficient. The red zone corresponds to the disk and the blurred red zones correspond to the accretion column. The dashed blue line corresponds to the stagnation surface, and the black dotted line to the slow-magneto-sonic transition, the black dashed line corresponds to the Alfvénic transition. The dashed orange line corresponds to the position of the inner and outer light cylinders.

A Kerr space-time has two Killing vectors, $\boldsymbol{\eta} = (1/c)\boldsymbol{\partial_t}$ and $\boldsymbol{\xi} = \boldsymbol{\partial_\varphi}$ associated to stationarity and axisymmetry of this space-time. We will use the Boyer-Lindquist time coordinate t, to construct the 3+1 foliation of the Kerr space-time,

$$\mathcal{M} = \bigcup_{t\in\mathbb{R}}\Sigma_t \quad \text{where} \quad \Sigma_t = \{M\in\mathcal{M}\mid t(M) = t\}\,.$$

This foliation implies the existence of a fiducial observer whose 4-velocity is aligned with the direction of the t gradient. For a circular space-time as the Kerr space-time [Gourgoulhon (2010)], this fiducial observer is called the zero-angular-momentum observer (ZAMO). The ZAMO 4-velocity of the Kerr space-time is,

$$\mathbf{n} = \frac{1}{h}\left(\boldsymbol{\eta} - \boldsymbol{\beta}\right)\,, \tag{2}$$

where $h = \dfrac{\mathrm{d}\tau}{\mathrm{d}t}$ is the lapse function converting Boyer-Lindquist time to ZAMO proper time,

$$h = \left(1 - \frac{r_sr}{\rho^2} + \beta^\varphi\beta_\varphi\right)^{1/2} = \frac{\rho}{\Sigma}\sqrt{\Delta}\,, \tag{3}$$

and $\boldsymbol{\beta} = -\dfrac{\omega}{c}\boldsymbol{\partial}_\varphi$ is the shift vector of the ZAMO, where ω is the ZAMO shift pulsation.

For convenience, we also introduce an orthonormal basis $(\mathbf{n},\mathbf{e}_r,\mathbf{e}_\theta,\mathbf{e}_\varphi)$ associated with the natural base $(\partial_t,\partial_r,\partial_\theta,\partial_\varphi)$,

$$h_r\mathbf{e}_r = \boldsymbol{\partial}_r\,, \quad h_\theta\mathbf{e}_\theta = \boldsymbol{\partial}_\theta\,, \quad h_\varphi\mathbf{e}_\varphi = \boldsymbol{\partial}_\varphi\,, \tag{4}$$

with,

$$h_r = \frac{\rho}{\sqrt{\Delta}}\,, \quad h_\theta = \rho\,, \quad h_\varphi = \varpi\,. \tag{5}$$

This frame is associated to the ZAMO observer everywhere outside of the black hole horizon. Nevertheless $\mathbf{n}$ becomes singular on the horizon and cannot represent the four-speed of an observer. Then the physical interpretation of a non-invariant quantity like a vector field component is not obvious on the horizon. We introduce for the components of each vector $\mathbf{A}$ the notation,

$$\mathbf{A} = A^\mu \boldsymbol{\partial}_\mu = A^{\hat{\mu}} \mathbf{e}_\mu\,. \tag{6}$$

We also denote by $H = \{M \in \mathcal{M} \,|\, r(M) = r_H\}$ the black hole horizon where we have, $r_H = r_g\left(1+\sqrt{1-a^2}\right)$.

1.2 Particle number continuity

Here, we consider a scenario where highly energetic photons or relativistic neutrinos, which are in the very close black hole vicinity, load the magnetosphere with electron-positron plasma via the mechanism of pair creation,

$$\gamma + \gamma \rightleftharpoons e_+ + e_-\,, \tag{7}$$

$$\nu + \bar{\nu} \rightleftharpoons e_+ + e_-\,. \tag{8}$$

In the following, we refer to neutrinos or photons as the radiative component and index quantities linked to these with $_r$. In a medium composed of radiation and leptonic plasma, the mechanism of pair creation implies a modified expression of the particle number continuity equation. For electrons and positrons, Eqs. (7) and (8) we get, respectively,

$$\nabla\cdot n_+\mathbf{u}_+ = \frac{1}{c}\frac{\delta^4 n_+^{\text{created}}}{\delta^3\mathcal{V}_{\mathbf{u}_+}\delta\tau_+}\,, \quad \nabla\cdot n_-\mathbf{u}_- = \frac{1}{c}\frac{\delta^4 n_-^{\text{created}}}{\delta^3\mathcal{V}_{\mathbf{u}_-}\delta\tau_-}\,, \tag{9}$$

where n_- (n_+) is the electron (positron) number density, $\mathbf{u}_-$ ($\mathbf{u}_+$) the 4-velocity of the electron (positron) fluid, $\delta^3\mathcal{V}_{\mathbf{u}_-}$ (or $\delta^3\mathcal{V}_{\mathbf{u}_+}$) is the elementary volume in the reference frame of the electron (positron) fluid, $\delta\tau_+$ ($\delta\tau_-$) is the positron (electron) fluid proper time and $\delta^4 n_-^{\text{created}}$ ($\delta^4 n_+^{\text{created}}$) is the total injection of electrons (positrons) due to photon or neutrino annihilation in the respective elementary time and volume.

For each process, Eq. (7) or (Eq. 8), the number of created electrons is equal to the number of created positrons, which is also equal to the number of disappearing photons for the first process, Eq. (7) or neutrinos for the second one, Eq. (8). This exchange of different components implies that the electron-positron fluid component $\rho_0\mathbf{u}\hat{=}m_e\,(n_+\mathbf{u}_+ + n_-\mathbf{u}_-)$ is no longer conserved,

$$\nabla\cdot(\rho_0\mathbf{u} + m_e\mathbf{N}_r) = 0 \quad \overset{\text{3+1 formalism}}{\Longrightarrow} \quad \boldsymbol{\nabla}\cdot\rho_0 h\gamma\mathbf{V}_p = chk_m\,, \tag{10}$$

where $\boldsymbol{\nabla}$ indicates the covariant derivative on the spatial Σ_t manifold, $\mathbf{N}_r$ is the Feynman number 4-current of radiative component and ρ_0 is the mass density in the electron-positron fluid reference frame. The second equation derives from the steadiness and axisymmetry assumptions.

The term $ck_m = \dfrac{\delta^4 m^{\text{created}}}{\delta^3\mathcal{V}_{\mathbf{u}}\delta\tau_{\mathbf{u}}}$ in Eq. (9) and Eq.(10) corresponds to the rate of the created electron-positron mass per unit volume measured in the fluid reference frame and per fluid proper time unit. $\delta^3\mathcal{V}_{\mathbf{u}}$ is the elementary volume in the fluid reference frame and $\delta\tau_{\mathbf{u}}$ is the elementary proper time.

Then, chk_m is the rate of created electron-positron mass per unit volume measured by the ZAMO and per unit time in the Boyer-Lindquist coordinates. We have,

$$chk_m = -cm_e h\,\nabla\cdot\mathbf{N}_r = \frac{\delta^4 m^{\text{created}}}{\delta^3\mathcal{V}_{\text{ZAMO}}\delta t}\,. \tag{11}$$

We remind that $\delta^3\mathcal{V}_{\mathbf{u}} = \gamma\delta^3\mathcal{V}_{\text{ZAMO}}$, $\delta\tau = \gamma\delta\tau_{\mathbf{u}}$ and $\delta\tau = h\delta t$.

1.3 4-current and Maxwell's equations

For both pair creation processes the initial particles are not charged, so the source terms of the electromagnetic field $\mathbf{j}$ are due only to the electron-positron plasma, $\mathbf{j} = e\,(n_+\mathbf{u}_+ - n_-\mathbf{u}_-)$. Hence, the 3+1 decomposition of Maxwell's equations in a Kerr space-time maintains their ordinary expressions,

$$\boldsymbol{\nabla}\cdot\mathbf{E} = 4\pi\rho_e\,, \tag{12}$$

$$\boldsymbol{\nabla}\cdot\mathbf{B} = 0\,, \tag{13}$$

$$\boldsymbol{\nabla}\times(h\mathbf{E}) = \left(\mathbf{B}\cdot\boldsymbol{\nabla}\frac{\omega}{c}\right)\varpi\mathbf{e}_\varphi\,, \tag{14}$$

$$\boldsymbol{\nabla}\times(h\mathbf{B}) = \frac{4\pi h}{c}\mathbf{J} - \left(\mathbf{E}\cdot\boldsymbol{\nabla}\frac{\omega}{c}\right)\varpi\mathbf{e}_\varphi\,, \tag{15}$$

where ρ_e is the electric charge density and $\mathbf{J}$ the charged current measured by the ZAMO $\mathbf{j} = \rho_e\mathbf{n} + \mathbf{J}$. We also assume infinite electrical conductivity,

$$\mathbf{E} + \frac{\mathbf{V}\times\mathbf{B}}{c} = 0\,. \tag{16}$$

1.4 Euler's equation and effective enthalpy equation

The momentum and the energy equations, respectively the Euler's equation and the first law of thermodynamics, are obtained using the 3+1 decomposition of the energy-momentum conservation. Here our energy-momentum tensor is composed of the electro-magnetic part $\mathbf{T}_{\text{EM}}$, the electron-positron part $\mathbf{T}_{\text{FL}}$ and the radiative part $\mathbf{T}_r$. We note that $\mathbf{T}_{\text{MHD}} = \mathbf{T}_{\text{FL}} + \mathbf{T}_{\text{EM}}$ is the MHD part of the energy-momentum tensor and $\mathbf{k} = -\nabla\cdot\mathbf{T}_r = \nabla\cdot\mathbf{T}_{\text{MHD}}$ is the 4-force exerted by radiation on the fluid of pairs. It may also include Compton or Inverse-Compton forces due to pair creation. We will focus our attention on the motion and dynamics of the electron-positron fluid. We make the additional assumption that the distribution function of the considered electron-positron plasma $(m_+ + m_-)f = m_+f_+ + m_-f_-$ is isotropic in velocity around a fluid reference frame four velocity $\mathbf{u}$. It implies that if we decompose the four-velocity in the fluid reference frame $\mathbf{u}_P = \gamma_P\,(\mathbf{u} + \mathbf{W}_P/c)$, then for each position in space-time we have $f(\mathbf{u}_P) = f\,(||\mathbf{W}_P||)$. With these assumptions the energy-momentum of the pair plasma is,

$$\mathbf{T}_{\text{FL}} = \rho_0\xi c^2\mathbf{u}\otimes\mathbf{u} + P\mathbf{g}\,, \tag{17}$$

where P is an effective pressure. Here, the effective enthalpy per unit mass in the fluid frame ξ, which plays a role in the fluid inertia, differs from that obtained for ideal fluids with relativistic temperatures, in thermodynamical equilibrium. We have $\xi_{\text{eq}}(\Theta)$ (where $\Theta = P/\rho_0c^2$ the dimensionless temperature, given by Synge law (see Synge 1957, Chernikov 1963, Marle 1969) or the Taub-Matthews equation of state (see Mathews 1971). The difference $\delta e/c^2 = \xi - \xi_{\text{eq}}(\Theta)$ is positive where the wings of the distribution function are larger than those of thermodynamics equilibrium fluid and negative in the reverse case. For more details see part 3.3.2 of Chantry (2018).

From the previous equations, we deduce the 3+1 decomposition,

$$\rho_0\gamma\left(\mathbf{V}\cdot\boldsymbol{\nabla}\right)\left(\gamma\xi\mathbf{V}\right)+\quad\rho_0\xi\gamma^2\left[c^2\boldsymbol{\nabla}\ln h+\frac{\varpi\omega V^{\hat{\varphi}}}{h}\boldsymbol{\nabla}\ln\omega\right]+\boldsymbol{\nabla}P$$
$$=\rho_e\mathbf{E}+\frac{\mathbf{J}\times\mathbf{B}}{c}+\left(\mathbf{k}\cdot\mathbf{n}\right)\mathbf{n}+\mathbf{k}-\gamma\xi ck_m\mathbf{V}\,, \tag{18}$$

where $\mathbf{V}$ is the speed of the electron-positron fluid measured by the ZAMO. Note that the mechanism of pair creation produces forces on the electron-positron fluid. One force comes from the direct effect of the radiative components, the second one comes from the variation of the inertia due to the transformation. In Huang et al. (2019) the assumption is added that in our notations reads $\mathbf{k}=c^2\left(\nabla\cdot\rho_0\mathbf{u}\right)\mathbf{u}$. This assumption leads to some differences in the treatment of the matching conditions compared to ours, as we will see below.

The projection of the conservation of energy-momentum equation along the electron-positron fluid 4-velocity in the comoving frame finally gives,

$$\rho_0\left(\mathbf{V}_\mathrm{p}\cdot\boldsymbol{\nabla}\right)\left(\xi c^2\right)=\left(\mathbf{V}_\mathrm{p}\cdot\boldsymbol{\nabla}\right)P-\frac{c}{\gamma}\mathbf{k}\cdot\mathbf{u}\,. \tag{19}$$

The additional term $\frac{c}{\gamma}\mathbf{k}\cdot\mathbf{u}$ corresponds to the way the injection of pairs contributes to the effective internal enthalpy.

1.5 Integrals of motion

The first integrals derived from Maxwell equations in Chantry et al. (2018) are still valid here because those equations are not modified by the introduction of pair production. Thus, because of axisymmetry, magnetic flux conservation can be written,

$$\mathbf{B}_\mathrm{p}=\frac{\boldsymbol{\nabla}A\times\mathbf{e}_\varphi}{\varpi}\,, \tag{20}$$

with $\partial_\varphi A=0$. Faraday's induction law (Eq. 14) leads immediately to the existence of an electrical potential Φ, such that $h\mathbf{E}=\frac{\omega}{c}\nabla A-\nabla\Phi$. Axisymmetry also implies that $\partial_\varphi\Phi=0$. From the symmetries and Ohm's law for infinite electrical conductivity, Eq. (16), we deduce that the poloidal velocity and the poloidal magnetic field are aligned. Hence, there is a function Ψ_A such that,

$$\Psi_A\mathbf{B}_p=4\pi\rho_0h\gamma\mathbf{V}_p\,. \tag{21}$$

Inserting this result into Eq. (10) we can interpret Ψ_A as the mass flux per unit magnetic flux on a given magnetic flux tube. Combining the continuity equation, Eq. (10), the divergence-free property of the magnetic field , Eq. (13) together with the previous equation we get,

$$\mathbf{B}_p\cdot\nabla\Psi_A=4\pi ch k_m\,, \tag{22}$$

which governs how the mass flux per unit of magnetic flux Ψ_A varies along a poloidal field line. Together with Ohm's law, Eq. (16), we get,

$$c\nabla\Phi=\left[\omega+\frac{1}{\varpi}\left(hV^{\hat{\varphi}}-\frac{\Psi_AB^{\hat{\varphi}}}{4\pi\rho_0\gamma}\right)\right]\nabla A\,.$$

The "electrical" potential Φ is then a function of the magnetic flux function A, $\Phi=\Phi(A)$. We may introduce the so-called frequency of isorotation, which is a function of the magnetic flux,

$$\Omega(A)\equiv c\frac{d\Phi}{dA}\ \text{ with }\ \mathbf{E}=-\frac{\Omega-\omega}{hc}\nabla A\,. \tag{23}$$

We introduce the poloidal Mach number,

$$M^2_\mathrm{Alf}=h^2\frac{{V_\mathrm{p}}^2}{V^2_\mathrm{Alf}}=\frac{4\pi h^2\rho_0\xi\gamma^2{V_\mathrm{p}}^2}{{B_\mathrm{p}}^2}=\frac{\xi{\Psi_A}^2}{4\pi\rho_0}\,. \tag{24}$$

Following Lasota et al. (2014), we calculate Noether's current densities associated to the two space-time Killing vectors,

$$\mathbf{M}_\mathrm{MHD}=\ \mathbf{T}_\mathrm{MHD}(\,.\,,\boldsymbol{\xi})\,, \tag{25}$$
$$\mathbf{P}_\mathrm{MHD}=-\mathbf{T}_\mathrm{MHD}(\,.\,,\boldsymbol{\eta})\,. \tag{26}$$

$\mathbf{M}_\mathrm{MHD}$ ($\mathbf{P}_\mathrm{MHD}$) corresponds respectively to the Noether's current density, also called fluxes, associated with the symmetry generator $\boldsymbol{\xi}$ ($\boldsymbol{\eta}$). In what follows, we will refer to these quantities as the Noether's angular momentum and energy current or flux of the MHD part of the energy-momentum tensor.

From Eq. (17), the previous equation and the usual 3+1 decomposition of the electromagnetic energy-momentum tensor allow to get the poloidal component of these Noether's current densities,

$$h\mathbf{M}_\mathrm{MHD,p}=\frac{\Psi_AL}{4\pi c}\mathbf{B}_p\,, \tag{27}$$
$$h\mathbf{P}_\mathrm{MHD,p}=\frac{\Psi_A\mathcal{E}}{4\pi c}\mathbf{B}_p\,, \tag{28}$$

where,

$$L=\varpi\left(\gamma\xi V^{\hat{\varphi}}-\frac{hB^{\hat{\varphi}}}{\Psi_A}\right)\,, \tag{29}$$

$$\mathcal{E}=\gamma\xi hc^2\left(1+\frac{\varpi\omega V^{\hat{\varphi}}}{hc^2}\right)-\frac{h\varpi\Omega}{\Psi_A}B^{\hat{\varphi}}\,, \tag{30}$$

are the usual specific angular momentum and specific energy. Using $\mathbf{k}=\nabla\cdot\mathbf{T}_\mathrm{MHD}$ and the Killing vector definition we get,

$$\nabla\cdot\left(h\mathbf{M}_\mathrm{MHD,p}\right)=\ h\mathbf{k}\cdot\boldsymbol{\xi}\,, \tag{31}$$
$$\nabla\cdot\left(h\mathbf{P}_\mathrm{MHD,p}\right)=-h\mathbf{k}\cdot\boldsymbol{\eta}\,, \tag{32}$$

which leads to,

$$\mathbf{B}_p\cdot\boldsymbol{\nabla}\left(\Psi_AL\right)=4\pi h(\mathbf{k}\cdot\boldsymbol{\xi})\,, \tag{33}$$
$$\mathbf{B}_p\cdot\boldsymbol{\nabla}\left(\Psi_A\mathcal{E}\right)=-4\pi ch(\mathbf{k}\cdot\boldsymbol{\eta})\,. \tag{34}$$

Those equations describe how the angular momentum and energy flux of the MHD fields evolve along a poloidal field line. Thus the mass flux, the angular momentum and the energy of the fluid plus the electromagnetic fields are loaded by the mechanism of pair creation. Therefore the isorotational functions remains a constant along a poloidal field line.

1.6 Energetic balance on the black hole horizon

It is well known that a Kerr black hole can transfer part of its rotational energy to its environment. The processes of Penrose & Floyd (1971) and Blandford & Znajek (1977) explain how a Kerr black hole may transfer part of its rotational energy to particles, or the electromagnetic field. Penrose's process involves particles and Blandford-Znajek's process force-free MHD fields obtained by a perturbation method, expanding the spin for radial or paraboloidal fields. In fact, the black hole may transfer angular momentum and rotational energy to the plasma, as explained and discussed in Lasota et al. (2014).

In our configuration, we consider the interaction between the non force-free magnetised fluid and the black hole. We neglect how the radiation exchanges energy and angular momentum with the Kerr black hole. The exchange of rotational energy of angular momentum is determined by the value of the $\mathbf{T}_\mathrm{MHD}$ tensor at the horizon of the black hole. As in Lasota et al. (2014), we can integrate Noether's flux conservation equations Eqs. (31) - (32), or the equivalent system, but this time in the volume of space-time between two neighbouring flux tubes $\mathcal{T}_A$ and $\mathcal{T}_{A+\mathrm{d}A}$ anchored on the horizon of the black hole (see Fig. 2). This integration is performed for radii between r_H and

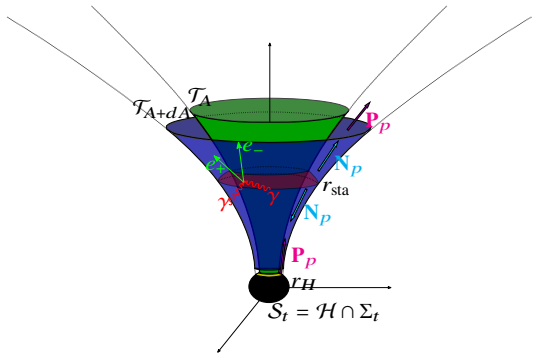

Figure 2. Schematic representation of two neighbouring flux tubes $\mathcal{T}_A$ and $\mathcal{T}_{A+dA}$ anchored in the black hole horizon at the r_H radius. The stagnation surface is defined as the surface with null poloidal speed ($V_p = 0$). It is the red disk labelled with $r_{\rm sta}$. N_p and P_p are the poloidal fluxes of particle and Noether's energy in the outflow and inflow.

$r > r_H$ and for a time interval between t and $t + \mathrm{d}t$. In fact, we could directly integrate Eqs. (33)-(34) and also Eq. (22) along a poloidal field line anchored into the black hole (see Fig. 2),

$$\frac{\mathrm{d}\dot{M}}{\mathrm{d}A} = \Psi_{A,H}\,(A) + \int_0^\ell \left.\frac{4\pi hck_m}{||\,\mathbf{B}_{\rm p}\,||}\right|_{A=\rm cst} \mathrm{d}\ell\,, \tag{35}$$

$$\Psi_A L = \Psi_{A,H} L_H\,(A) + \int_0^\ell \left.\frac{4\pi h\mathbf{k}\cdot\boldsymbol{\xi}}{||\,\mathbf{B}_{\rm p}\,||}\right|_{A=\rm cst} \mathrm{d}\ell\,, \tag{36}$$

$$\Psi_A \mathcal{E} = \Psi_{A,H}\mathcal{E}_H\,(A) - \int_0^\ell \left.\frac{4\pi hc\mathbf{k}\cdot\boldsymbol{\eta}}{||\,\mathbf{B}_{\rm p}\,||}\right|_{A=\rm cst} \mathrm{d}\ell\,. \tag{37}$$

These equations are easily interpreted, since the mass flux, the angular momentum and the energy, per unit magnetic flux, at a given point of a poloidal field line are composed of the contribution of the black hole and the injection of mass, angular momentum and energy, respectively, due to the radiation.

Horizon is a one-way hyper-surface, then $\Psi_{A,H} < 0$. Energy is extracted from the black hole if $\Psi_{A,H}\mathcal{E}_H\,(A) > 0$, which is equivalent to $\mathcal{E}_H < 0$. The black horizon absorbs negative energy per unit mass $\mathcal{E}_H$ (see also Toma & Takahara (2016)).

Then, following Christodoulou (1970) and Thorne (1987) the black hole physical parameters evolve in time, according to,

$$\frac{r_H - r_g}{2r_H r_g}\frac{d^2\mathrm{M_{irr}}c^2}{dtdA} = -\left(\Psi_{A,H}\mathcal{E}_H - \omega_H\Psi_{A,H}L_H\right)\,, \tag{38}$$

$$\frac{d^2\mathcal{J}}{dtdA} = -\Psi_{A,H}L_H\,, \tag{39}$$

$$\frac{d^2\mathrm{M}c^2}{dtdA} = -\Psi_{A,H}\mathcal{E}_H\,. \tag{40}$$

where $M_{\rm irr}$,

$$M_{\rm irr} = M\sqrt{\frac{1+\sqrt{1-a^2}}{2}}\,, \tag{41}$$

is the irreducible mass of the black hole. Here we apply the formulation given by Thorne (1987) to link the Noether's energy and angular momentum flux on the black hole horizon to the black hole parameter.

In order to interpret physically the energy, it is useful to decompose the energy flux in its different physical contributions,

$$\Phi_{\mathcal{E}} = \Psi_A\mathcal{E} = \Psi_A\gamma\xi hc^2\left(1 + \frac{\varpi\omega V^{\hat{\phi}}}{hc^2}\right) - h\varpi\Omega B^{\hat{\varphi}} = \Phi_{\rm FL} + \Phi_{\rm EM}\,. \tag{42}$$

The first term is the Noether energy flux of the fluid $\Phi_{\rm FL}$. The Noether Poynting flux $\Phi_{\rm EM}$ corresponds to the electromagnetic energy flux. The fluid term $\Phi_{\rm FL}$ is composed of two terms. The first term $\Phi_{\rm M} = \Psi_A\gamma\xi hc^2$ (negative on the black hole horizon) contains the absorption by the black hole of pure massive energy, plus the internal and the kinetic energy of the fluid. We must have $\gamma\xi \longrightarrow +\infty$ on the horizon in order to let $h\gamma\xi$ finite and non-zero. The second term is $\Phi_{\rm LT} = \Psi_A\gamma\xi\varpi\omega V^{\hat{\varphi}}$ that we call the Lense-Thirring term. It can be positive. Its sign will depend on the sign of $V^{\hat{\varphi}}$). Note also that the pair fluid contribution $\Phi_{\rm FL}$ can be re-wrote as,

$$\Phi_{\rm FL} = -\Psi_A\xi c^2\,(\mathbf{u}\cdot\boldsymbol{\eta})\,. \tag{43}$$

As a consequence, $\Phi_{\rm FL}$ can be positive in an inflow ($\Psi_A < 0$), only if $\boldsymbol{\eta}$ is not a time-like future oriented vector, that is to say in the ergo-region.

Blandford & Znajek (1977) show that under certain conditions the Poynting flux can be transported to infinity, meaning that the electromagnetic field is fed by the rotation energy of the Kerr black hole. We say that the *electromagnetic extraction process is active where* $\Phi_{\rm EM}|_H > 0$. *We also says that the pair fluid process is active where* $\Phi_{\rm FL}|_H = \Phi_{\rm M}|_H + \Phi_{\rm LT}|_H > 0$.

The null energy condition applying to $\mathbf{T}_{\rm MHD}$ on the horizon (see Lasota et al. 2014) writes,

$$\Phi_{\mathcal{E}}|_H \leq \Psi_A L|_H\,\omega_H\,, \tag{44}$$

which implies the impossibility of *generalised energy extraction* ($\Phi_{\mathcal{E}}|_H > 0$) for non rotating black hole. With regard to Eq.(38), this condition implies the increasing of the irreducible mass, which also implies an increase of the black hole entropy.

We can pursue the calculation of this decomposition, by inverting the motion integrals system on the black hole horizon. For the details of the inversion procedure, see Chantry et al. (2018). The result on the horizon is,

$$\Phi_{\rm M}\big|_H = -\frac{M^2_{\rm Alf}\big|_H}{M^2_{\rm Alf}\big|_H + \varpi_H^2(\Omega-\omega_H)^2/c^2}\left(\Psi_A L\omega_H - \Psi_A\mathcal{E}\right)\,, \tag{45}$$

$$\Phi_{\rm LT}\big|_H = \Psi_A L\omega_H + \frac{\varpi_H^2\omega_H(\Omega-\omega_H)/c^2}{M^2_{\rm Alf}\big|_H + \varpi_H^2(\Omega-\omega_H)^2/c^2}\left(\Psi_A L\omega_H - \Psi_A\mathcal{E}\right)\,, \tag{46}$$

$$\Phi_{\rm EM}\big|_H = \frac{\varpi_H^2\Omega(\omega_H-\Omega)/c^2}{M^2_{\rm Alf}\big|_H + \varpi_H^2(\Omega-\omega_H)^2/c^2}\left(\Psi_A L\omega_H - \Psi_A\mathcal{E}\right)\,, \tag{47}$$

where each quantity is evaluated on the black hole horizon.

We focus our attention on a generic field line. Let us now consider the case where injection on this line is entirely located on a point $r = r_I > r_H$. We also suppose that injection on this line is sufficient to have both an inflow ($\Psi_A \leq 0$ for $r < r_I$), and an outflow ($\Psi_A > 0$ for $r \geq r_I$). On this line there is no injection $k_m, \mathbf{k} = 0$ except at the injection point (black dot in the left part of Fig.2). We should now look at the conditions that the extractions process imposes on the position of the starting point, which is the injection point at $r_{\rm I}$.

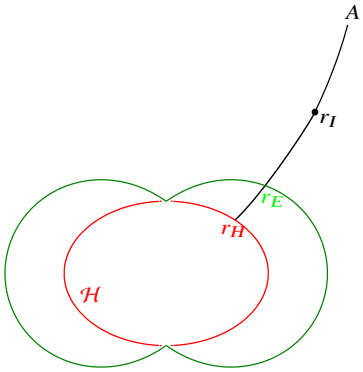

Figure 3. Representation of a typical poloidal velocity and magnetic field line. The injection of pairs is supposed to be located on the black dot outside the ergosphere, $r_I > r_E$. Without a magnetic field, energy extraction is impossible, if the injection point is outside the ergo-region.

In the case of a pure pair fluid, without electro-magnetic field, $\Phi_{\rm EM} = 0$, on the section of the poloidal field line going from the black hole to the location of injection ($r_H \leq r \leq r_{\rm I}$) (see Fig. 3), we have $\Psi_A = {\rm Cst} < 0$. In addition Eqs.(37 and 42) imply that for all $r \in]r_H; r_I[$ we have $\Psi_A \mathcal{E}(r) = \Phi_{\rm FL}(r) = {\rm Cst}$. In this case, the fluid extraction process cannot be active if the injection is located outside of the ergosphere. Indeed, if the injection starts outside of the ergosphere ($r_{\rm I} \geq r_{\rm E}$), then for a point outside of the ergosphere and below the injection point ($r_E \leq r \leq r_{\rm I}$) $\Phi_{\rm FL,H} = \Phi_{\rm FL}(r) = -\Psi_A \xi c^2 (\mathbf{u} \cdot \boldsymbol{\eta}) < 0$. In this zone, $-\Psi_A(r) > 0$ ($r < r_I$) and $(\mathbf{u} \cdot \boldsymbol{\eta}) < 0$ because outside of the ergosphere $\boldsymbol{\eta}$ is time-like and future oriented. This is equivalent to the necessity in the Penrose process to get the fission of the particles inside the ergosphere.

In the MHD case, we can have extraction via a process of fluid extraction and have a point of injection outside of the ergosphere because we can have exchange between the ideal fluid energy flux and the Poynting flux. Thus, in this case, the Poynting flux increases as one moves out of the ergosphere while the ideal fluid flux became positive inside the ergosphere, being negative outside of the ergosphere. Eq.47) implies that the electromagnetic process is active where $0 < \Omega < \omega_H$, which is a result already obtained by Blandford & Znajek (1977).

2 THE MODEL ON THE BLACK HOLE HORIZON AND ON THE PAIR CREATION LAYER

2.1 Symmetries of the model

In the Newtonian case ($\mu = l = 0$) or with a non rotating black hole $l = 0$ the system of equations in the appendix C of Chantry et al. (2018), ν and λ appears only with a square, and then is invariant under the transformation $\nu \longleftrightarrow -\nu$ or $\lambda \longleftrightarrow -\lambda$. This property is due to the symmetry of ideal, axisymmetric and stationary MHD equations in Newtonian gravity or around a Schwarzschild black hole. Nevertheless, in Kerr configuration the Lense-Thirring term breaks the previous symmetry. The model system of equations (Eqs (C.3) and (C.4) of Chantry et al. (2018)) is invariant under sign transformations preserving the product $\lambda\nu l$. Then the model system of equations is invariant under the following transformations,

$$\left\{\begin{array}{ccc} \lambda & \longleftrightarrow & -\lambda \\ \nu & \longleftrightarrow & -\nu \\ l & \longleftrightarrow & l \end{array}\right. , \quad \left\{\begin{array}{ccc} l & \longleftrightarrow & -l \\ \nu & \longleftrightarrow & -\nu \\ \lambda & \longleftrightarrow & \lambda \end{array}\right. \quad \text{or} \quad \left\{\begin{array}{ccc} l & \longleftrightarrow & -l \\ \lambda & \longleftrightarrow & -\lambda \\ \nu & \longleftrightarrow & \nu \end{array}\right. . \tag{48}$$

This question of symmetry of the various models is postponed in a future work.

2.2 Inflow/outflow model with a thin layer

A careful look of the self-similar model developed in Chantry et al. (2018) shows that it produces inflow and outflow solutions, starting from the radius where the poloidal velocity of the flow is zero. This radius defines the stagnation radius and the stagnation sphere.

We build inflow solution by taking negative values of ν. Taking ν negative means that we allow the value of $V_\star$ to be negative. Thus it becomes the radial component of velocity at the intersection of the Alfvén surface and the axis.

However ν negative is not sufficient to distinguish an inflow from an outflow one. A solution can be interpreted as a physical inflow only if it accelerates from the stagnation surface towards the black hole horizon, crossing first the slow magnetosonic surface and then the Alfvén/Fast magneto surface before reaching the horizon.

In order to describe the MHD field, from horizon to infinite, we need to use source of material to match under some continuity conditions (matching conditions) an inflow to an outflow. We propose here to link an outflow and an inflow solutions of the self-similar model, which have the same stagnation radius, with a thin injection (pair creation or other processes) layer at the level of the stagnation surface.

Indeed this means that the pair creation terms k_m and $\mathbf{k}$ are null *except at the stagnation surface of the solution* (a sphere). Similar kind of double flow are exposed in Globus & Levinson (2013) or Huang et al. (2019). In the following we will use the notations adopted in the Chantry et al. (2018) model. We also use $_{\rm in}$ and $_{\rm out}$ index to refer to a quantity calculated just down the stagnation radius (for inflow) and just up the stagnation radius (for outflow).

The electro-magnetic field source is only due to the electron-positron four-current. Nevertheless the creation of pairs or other processes on this thin layer can be at the origin of current and charge density in the layer, which will imply some discontinuity of some components of the electromagnetic fields. The surface electromagnetic sources are then located on the stagnation surface.

2.3 Matching conditions for both flows

First, let us consider some thin layer at the stagnation surface position ($r \in \left[r_{\rm sta} - \dfrac{\Delta r}{2}; r_{\rm sta} + \dfrac{\Delta r}{2}\right]$) where the pairs are created. The Maxwell-Flux Eq.(13), the Maxwell-Faraday Eq.(14) and the assumptions of axisymmetry and ideality (Eq.16) ensure the continuity of the magnetic flux and the isorotation function along the field line of magnetic field,

$$\left\{\begin{array}{l} \mathbf{B}_p \cdot \boldsymbol{\nabla} A = 0 \\ \mathbf{B}_p \cdot \boldsymbol{\nabla} \Omega = 0 \end{array}\right. \underset{\Delta r \to 0}{\Longrightarrow} \left\{\begin{array}{l} \left[A\left(r_{\rm sta}, \theta\right)\right]^{\rm out}_{\rm in} = 0 \\ \left[\Omega\left(r_{\rm sta}, \theta\right)\right]^{\rm out}_{\rm in} = 0 \end{array}\right. . \tag{49}$$

We require the same stagnation radius for both the inflow and the outflow, assuming $\Delta r \to 0$. Thus the two flows coincide on the stagnation surface,

$$r^{\rm out}_{\rm sta} = r^{\rm in}_{\rm sta} = r_{\rm sta} . \tag{50}$$

The stagnation surface is spherical. This induces a continuity of the radial magnetic field component $B^{\hat{r}}$ and, as a consequence, of $\partial_\theta A$. Thus, the integration of the Maxwell-Flux Eq. (13) on a infinitesimal volume around the stagnation surface leads that the magnetic field component $B^{\hat{r}}$, perpendicular to this surface, has to be continuous. It is equivalent to the continuity of $\partial_\theta A$,

$$[\partial_\theta A\,(\,r_{\rm sta}\,,\theta)]^{\rm out}_{\rm in} = 0\,. \tag{51}$$

Matching inflow and outflow solutions of the meridional self-similar model (Chantry et al. 2018), the continuity of $\partial_\theta A$ is directly obtained from the continuity of the magnetic flux (first line of Eq.49) and from,

$$A_{\rm in/out} = A_{\star{\rm in/out}} f_{\rm in/out}(R)\,\sin^2\theta\,. \tag{52}$$

Here R corresponds to the dimensionless radius $R = r/r_\star$, where $r_\star$ is the Alfvén radius. Finally, Eq.(51) does not add a matching constraint since it is equivalent to the continuity of the magnetic field component $B^{\hat{r}}$ across the stagnation layer.

In the same way, the integration of Maxwell-Faraday Eq.(14) on a small surface delimited by a small loop, using the continuity of the magnetic flux, induces that the latitudinal electric field component, $E^{\hat{\theta}}$, is also continuous on the stagnation layer. We may have a discontinuity of the derivative $\partial_r A$ on the stagnation layer, and this jump is due to the toroidal surface current flux, $J^{\hat{\varphi}}_\sigma$, and the surface charge density, σ_e. After integrating the Maxwell-Gauss Eq.(12) and the Maxwell-Ampere Eq.(15), we get,

$$\begin{cases} -\dfrac{\Omega-\omega}{hh_r c}\,[\partial_r A\,(\,r_{\rm sta}\,,\theta)]^{\rm out}_{\rm in} = & 4\pi\sigma_e\,, \\ \dfrac{1}{\varpi h_r}\,[\partial_r A\,(\,r_{\rm sta}\,,\theta)]^{\rm out}_{\rm in} = & \dfrac{4\pi}{c} J^{\hat{\varphi}}_\sigma\,, \end{cases} \tag{53}$$

where the surface current is defined by $J^{\hat{k}}_\sigma = \lim\limits_{\Delta r\to 0}\int_{r_{\rm sta}-\Delta r/2}^{r_{\rm sta}+\Delta r/2} J^{\hat{k}}{\rm d}r$, with $k = \theta$ or φ.

As in Chantry et al. (2018), the equations (Eqs.23,24,29,30) can be reversed in order to get the expression of the $B^{\hat{\varphi}}$ component as a function of the different physical quantities. The toroidal magnetic field is also linked to the intensity of the charges, which cross the surface inside a circle $C_{r,\theta} = \{M\in\Sigma\mid\theta(M)=\theta, r(M)=r\}$. In order to calculate the intensity of the charges across this surface per unit Boyer-Lindquist time t, we need to calculate the flux of $h\mathbf{J}$ across this surface. We use $h\mathbf{J}$ instead of $\mathbf{J}$ because the current flux $\mathbf{J}$ is calculated in the ZAMO proper time. Thus we are able to show, in the frame of our assumptions, that $I(r,\theta) = \int_{\mathcal{D}_{r,\theta}} h\mathbf{J}\cdot\mathbf{dS} = \frac{hc\,\varpi B^{\hat{\varphi}}}{2}$. Under axisymmetric and stationarity condition the poloidal electromagnetic Noether's flux can be expressed as $\mathbf{P}_{\rm EM,p} = -\frac{\varpi\Omega B^{\hat{\varphi}}}{4\pi c}\mathbf{B}_p = -\frac{I\Omega}{2\pi hc^2}\mathbf{B}_p$.

The matching conditions induced by possible electromagnetic surface sources do not impose the continuity of the global current intensity, I, across the stagnation surface. The current is also proportional to the Poynting flux per unit magnetic flux, $\Phi_{\rm EM} = -2\frac{\Omega I}{c}$). The global current can be expressed from the inversion of the motion integrals as it has been done in Chantry et al. (2018) using the cylindrical radius per unit of light cylinder radius, $x = \frac{\varpi(\Omega-\omega)}{hc}$. For the current we get,

$$\frac{2I}{c} = -\Psi_A L\left[1-\frac{M^2_{\rm Alf}+\frac{\varpi^2\Omega(\Omega-\omega)}{c^2}}{M^2_{\rm Alf}-h^2\left(1-x^2\right)}\right] - \frac{\Psi_A\mathcal{E}}{c^2}\,\frac{\varpi^2\,(\Omega-\omega)}{M^2_{\rm Alf}-h^2\left(1-x^2\right)}\,. \tag{54}$$

It implies that the continuity of the global current requires another constraint on how the injected angular momentum $\Delta\Psi_A L$ is related to the injected energy $\Delta\Psi_A\mathcal{E}$. Since there is no physical reason to have this requirement, our way of matching can support to have a discontinuity in the global current.

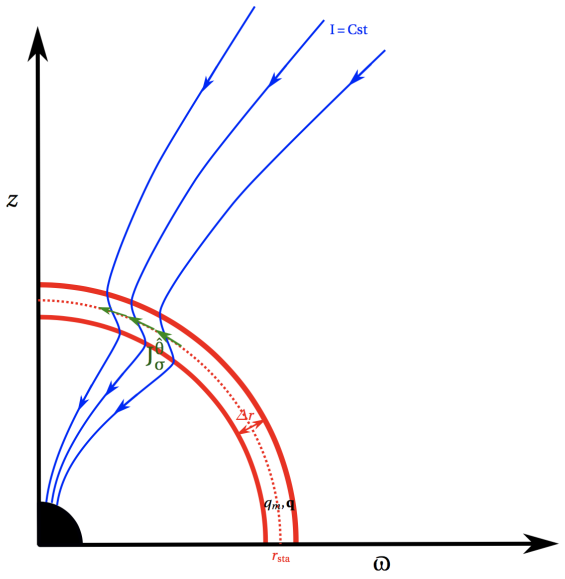

Figure 4. The current intensity $j^{\hat{\theta}}$ in the stagnation layer of thickness Δr creates a discontinuity of the global current function I.

Eqs.(22,33,34) imply the discontinuity of Ψ_A, $\Psi_A L$ and $\Psi_A\mathcal{E}$ on the stagnation layer. In other words the r.h.s of those three equations are zero except onto the stagnation surface itself where they are equal to a Dirac delta function. Thus from Eq.(54), we also get a discontinuity of the current intensity, I, which is equivalent to a discontinuity for $B^{\hat{\varphi}}$, becoming a discontinuity on the Poynting flux. It implies the presence of some meridional $J^{\hat{\theta}}_\sigma$ surface current.

A paradox seems to appear because charges may accumulate somewhere on the stagnation layer, due to the existence of non null $J^{\hat{\theta}}_\sigma$. To solve it, we use a schematic view of constant intensity I tube in the poloidal surface (see Fig. 4).

In our assumptions $\Delta r\to 0$ and we get a discontinuity of the intensity function, which implies a discontinuity of $hJ^{\hat{r}}$. It is linked to the variation with θ of the surface current $J^{\hat{\theta}}_\sigma$. Using the charge conservation, we can calculate the jump of the radial current at a co-latitude θ,

$$hJ^{\hat{r}}_{\rm in}\,(r_{\rm sta}) = hJ^{\hat{r}}_{\rm out}\,(r_{\rm sta}) + \frac{1}{\Sigma\sin\theta}\frac{\partial}{\partial\theta}\left(\rho\sin\theta J^{\hat{\theta}}_\sigma\right)\,. \tag{55}$$

Integrating this equation in order to let appear the discontinuity of the current function, we get,

$$I_{\rm in} = I_{\rm out} + 2\pi\rho(r_{\rm sta},\theta)\sin\theta J^{\hat{\theta}}_\sigma\,. \tag{56}$$

For each component of the flow, the parameters of the physical quantities are normalised to their own Alfvén radius. Thus, we need to adjust the two components of the flows, such that they correspond to a black hole of a given mass and spin. From the previous discussion, we also get a continuity of the isorotation function and the radial magnetic field component. Then, the matching conditions write,

$$\left[r_g\right]^{\rm out}_{\rm in} = 0,\quad [a]^{\rm out}_{\rm in} = 0,\quad [\Omega]^{\rm out}_{\rm in} = 0,\quad \left[B^{\hat{r}}\right]^{\rm out}_{\rm in} = 0. \tag{57}$$

The first three conditions combine with assumption Eq.(50) lead

to the three following jump conditions for the parameters,

$$\begin{cases} \left[\dfrac{R_{\rm sta}}{\mu}\right]_{\rm in}^{\rm out} = 0\,, \\ \left[\dfrac{l}{\mu}\right]_{\rm in}^{\rm out} = 0\,, \\ \left[\dfrac{\mu^3}{2\left(1+l^2\right)^2} + \dfrac{\lambda\mu^{3/2}}{\nu}\sqrt{1-\dfrac{\mu}{1+l^2}}\right]_{\rm in}^{\rm out} = 0\,. \end{cases} \tag{58}$$

We use those three conditions for numerical matching. Note that the third condition ensures the continuity of the isorotation function across the stagnation surface.

The last equation of Eqs. (57) and Eq. (50) relate the dimension of the Alfvén radius and magnetic field magnitude of the two flows,

$$\begin{cases} \dfrac{r_\star^{\rm in}}{r_\star^{\rm out}} = \dfrac{\mu_{\rm out}}{\mu_{\rm in}} \\ \dfrac{B_\star^{\rm in}}{B_\star^{\rm out}} = \left(\dfrac{\mu_{\rm in}}{\mu_{\rm out}}\right)^2 \dfrac{f_{\rm out}}{f_{\rm in}} \end{cases} \tag{59}$$

The second equation ensures the continuity of the magnetic flux. It imposes the ratio between $B_\star^{\rm in}$ and $B_\star^{\rm out}$ without bringing any extra constraint. As already seen above, the continuity of the radial magnetic field component Eq.(51) is directly derived from the continuity of the magnetic flux in our model.

Here we do not impose continuity of the Poynting flux between the inflow and the outflow because pair creation can induce the production of Poynting flux. Discontinuity of the Poynting flux is equivalent to discontinuity of the total current intensity I (see Fig. 4).

2.4 Energetic balance at the stagnation surface

Once, we have the inflow and outflow solutions from our semi-analytical model, which satisfy the system of Eqs.(58), we deduce the mass injection rate k_m of the pair creation and the 4-force $\mathbf{k}$ of the radiation field on the fluid of pairs. This includes the Compton, inverse Compton and pair creation. These terms take the following forms,

$$k_m = k_{m,\rm sta}\left(\theta\right)\delta\left(r-r_{\rm sta}\right)\,, \tag{60}$$

$$\mathbf{k} = \mathbf{k}_{\rm sta}\left(\theta\right)\delta\left(r-r_{\rm sta}\right)\,. \tag{61}$$

The integration on the stagnation surface of Eqs.22, 33 and34 gives the variation of the mass, angular momentum and energy fluxes. On the stagnation surface we get the following system,

$$\Psi_A^{\rm out}\left(A\right) = \Psi_A^{\rm in}\left(A\right) + \frac{4\pi chh_r}{B^{\hat{r}}}k_{m,\rm sta}\left(\theta_{\rm sta}\left(A\right)\right)\,, \tag{62}$$

$$\left(\Psi_A L\right)^{\rm out}\left(A\right) = \left(\Psi_A L\right)^{\rm in}\left(A\right) + \frac{4\pi hh_r}{B^{\hat{r}}}\boldsymbol{\xi}\cdot\mathbf{k}_{\rm sta}\left(\theta_{\rm sta}\left(A\right)\right)\,, \tag{63}$$

$$\left(\Psi_A \mathcal{E}\right)^{\rm out}\left(A\right) = \left(\Psi_A \mathcal{E}\right)^{\rm in}\left(A\right) - \frac{4\pi chh_r}{B^{\hat{r}}}\boldsymbol{\eta}\cdot\mathbf{k}_{\rm sta}\left(\theta_{\rm sta}\left(A\right)\right)\,. \tag{64}$$

In the outflow, the mass flux is positive, i.e. directed outwards, whereas in the inflow, it is negative, i.e. directed inwards. Applying the first condition to Eq.62 implies that for each colatitude we have $\frac{4\pi ch}{B^{\hat{r}}}k_{m,\rm sta}\left(\theta\left(A\right)\right) \geq \left(-\Psi_A^{\rm in}\left(A\right)\right)$, which means that the rate of pair creation needs to be sufficient to reverse the mass flux. The mass, angular momentum and energy injected per unit time and per unit dimensionless magnetic flux α, evaluated for the inflow solution, are given by the following expressions,

$$\frac{{\rm d}^2 M_{\rm Inj}}{{\rm d}t{\rm d}\alpha} = \dot{M}_{\rm Inj}^\star\frac{4}{\mu_{\rm out}^2}\left(\frac{G_{\rm out}}{G_{\rm in}}\right)^4\left[\frac{c\Psi_A^{\rm out}}{B_\star^{\rm out}} - \left(\frac{G_{\rm in}^2}{G_{\rm out}^2}\right)\frac{c\Psi_A^{\rm in}}{B_\star^{\rm in}}\right]\,, \tag{65}$$

$$\frac{{\rm d}^2 J_{\rm Inj}}{{\rm d}t{\rm d}\alpha} = \dot{J}_{\rm Inj}^\star\frac{8}{\mu_{\rm out}^3}\left(\frac{G_{\rm out}}{G_{\rm in}}\right)^4\left[\frac{\Psi_A^{\rm out}L_{\rm out}}{B_\star^{\rm out}r_\star^{\rm out}} - \left(\frac{\mu_{\rm out}G_{\rm in}^2}{\mu_{\rm in}G_{\rm out}^2}\right)\frac{\Psi_A^{\rm in}L_{\rm in}}{B_\star^{\rm in}r_\star^{\rm in}}\right]\,, \tag{66}$$

$$\frac{{\rm d}^2 E_{\rm Inj}}{{\rm d}t{\rm d}\alpha} = \dot{E}_{\rm Inj}^\star\frac{4}{\mu_{\rm out}^2}\left(\frac{G_{\rm out}}{G_{\rm in}}\right)^4\left[\frac{\Psi_A^{\rm out}\mathcal{E}_{\rm out}}{B_\star^{\rm out}c} - \left(\frac{G_{\rm in}^2}{G_{\rm out}^2}\right)\frac{\Psi_A^{\rm in}\mathcal{E}_{\rm in}}{B_\star^{\rm in}c}\right]\,, \tag{67}$$

with the following constants for the injection,

$$\dot{M}_{\rm Inj}^\star = \frac{{r_g}^2 {B_\star^{\rm in}}^2}{2c}\,,\quad \dot{J}_{\rm Inj}^\star = \frac{{r_g}^3 {B_\star^{\rm in}}^2}{2}\,,\quad \dot{E}_{\rm Inj}^\star = \frac{c{r_g}^2 {B_\star^{\rm in}}^2}{2}\,. \tag{68}$$

To get an order of magnitude for these quantities, we need the black hole mass and the value of the magnetic field at the Alfvén surface on the axis for the outflow $B_\star^{\rm out}$. For M87 the mass of the supermassive black hole is $M_H \approx (6.6\pm0.4)\times10^9 M_\odot$ (Gebhardt et al. 2011). On the axis of the M87 jet, Kino et al. (2014) give at the distance of $20r_g$ a magnetic field of the order of few Gauss, $B(20r_g) \approx 5\pm4\,$G. In our model, along the axis $B^r = B_\star/G^2$ (see Chantry et al. 2018). We restrain ourselves to solutions with $r_{\rm sta} < 20r_g$. In a recent publication, the Event Horizon Telescope Collaboration uses polarised emission imaging to estimate the magnetic field. They obtain a typical value of $B \approx 1-30\,$G in the region near the horizon. They also use a one-zone isothermal sphere model to estimate the magnitude of the magnetic field and get $\approx 5\,$G at $5r_g$. For solutions with $r_{\rm sta} < 5r_g$ we prefer to use the last observational constrain to fix the value of $B_\star^{\rm out}$. Then $B_\star^{\rm in}$ is calculated using the last equation of Eq.(59).

Since the fluxes are conserved in the inflow, along a given magnetic field line, which crosses the horizon of the black hole, and using Eqs.39 and 40), the fluxes are related to the variations of the black hole mass, angular momentum and energy. This writes,

$$\left(\Psi_A L\right)^{\rm out}\left(A\right) = -\frac{d^2 J_{\rm H}}{dtdA}\left(\theta_{\rm H}\left(A\right)\right) + \frac{4\pi h}{B^{\hat{r}}}\xi\cdot\mathbf{k}_{\rm sta}\left(\theta_{\rm sta}\left(A\right)\right)\,, \tag{69}$$

$$\left(\Psi_A \mathcal{E}\right)^{\rm out}\left(A\right) = -\frac{d^2 M_{\rm H}c^2}{dtdA}\left(\theta_{\rm H}\left(A\right)\right) - \frac{4\pi ch}{B^{\hat{r}}}\eta\cdot\mathbf{k}_{\rm sta}\left(\theta_{\rm sta}\left(A\right)\right)\,. \tag{70}$$

Thus for a line, which crosses the black hole horizon, the flux at infinity is constituted from the flux given by extraction from the black hole and the flux given by the photons which are transformed into pairs.

In the frame of the model proposed by Chantry et al. (2018), the rate at which energy is extracted from the rotating black hole is,

$$-\frac{dE_H}{dt} = \int_0^{A_H}\Psi_A\mathcal{E}dA = B_{\star,\rm in}^2 r_s^2 c\frac{h_\star^2\nu}{2\mu^{3/2}}\dot{w}\left(\alpha_H,\delta,e_1\right)\,, \tag{71}$$

with,

$$\dot{w}\left(\alpha_H,\delta,e_1\right) = \frac{2}{3\delta}\left\{\left(1+\delta\alpha_H\right)^{3/2}\left(1+\frac{3e_1\alpha_H}{5}-\frac{2e_1}{5\delta}\right)-1+\frac{2e_1}{5\delta}\right\}$$
$$\underset{\delta\to0}{\approx}\alpha_H+\frac{e_1\alpha_H^2}{2}+\frac{\delta\alpha_H^2}{4}\left(1+\frac{2e_1\alpha_H}{3}\right)\,.$$

Solution		λ	κ	δ	ν	l	μ	$\Pi_\star$	e_1
M1	I1	0.036	0.468	0.075	−1.79	0.12	0.442	1.4	−0.21
	O1	0.985	0.230	1.328	0.386	1.016×10^{-2}	3.758×10^{-2}		6.892×10^{-3}
M2	I2	0.392	1.341	0.355	−1.562	0.17	0.807	0.859	−0.349
	O2	0.998	0.280	1.296	0.234	6.502×10^{-3}	3.012×10^{-2}		6.892×10^{-3}
M3	I3	0.388	5.898	0.259	−1.443	0.25	0.978	0.275	−0.555
	O3	1.171	0.291	1.319	0.600	4.767×10^{-2}	0.184		$-6,268\times10^{-2}$

Table 1. Input parameters for the three solutions. For each of them, the first line presents the parameters for the inflow solution and the second line the parameters for the outflow solutions. The parameter λ is the dimensionless ratio of angular momentum flux per unit of magnetic flux. The parameter κ is the deviation from spherical symmetry of the pressure, while δ is the deviation from spherical symmetry of the number density/enthalpy ratio. ν is the escape speed per unit velocity of the fluid at the Alfvén point, along the polar axis. l is the dimensionless black hole spin and μ the Schwarzschild radius per unit Alfvén radius. $\Pi_\star$ is the dimensionless pressure at the Alfvén point along the polar axis and e_1 the deviation from spherical symmetry of the total energy.

Solution		a	Ω/ω_H	$r_{\rm sta}/r_{\rm H}$	$\gamma_{\rm max,ax}$	$\xi_\star$
M1	I1	0.5429	6.2167×10^{-2}	3.1777	15	3430
	O1	0.5410	6.2047×10^{-2}	3.1771	1.47	1.42
M2	I2	0.4316	9.6912×10^{-2}	1.5031	11	1360
	O2	0.4316	9.6912×10^{-2}	1.5031	4	1.5
M3	I3	0.5189	0.5022	1.1755	12	1470
	O3	0.5189	0.5022	1.1750	10	19.6

Table 2. We give a the dimensionless black hole spin, Ω/ω_H the dimensionless isorotation frequency and $r_{\rm sta}/r_H$ the dimensionless stagnation radius using minimal matching conditions, for the three solutions M1, M2 and M3. The two last columns give the maximum Lorentz factor along the fluid axis and the effective enthalpy $\xi_\star$ at the Alfvén point, on the polar axis.

3 DOUBLE FLOW SOLUTIONS

3.1 Parameters of three matching solutions

As explained in Chantry et al. (2018), a complete solution is fully determined by eleven parameters. Eight of them ($\lambda, \kappa, \delta, \nu, l, \mu, \Pi_\star$ and e_1) are the input parameters, which are required to solve the ordinary differential equations system (see Appendix C of Chantry et al. 2018). For the outflow solution, the $\Pi_\star$ value is automatically adapted by lowering its value to the limiting value to avoid oscillations in the jet. Thus the non-oscillating outflows are determined by seven input parameters. Conversely, inflows are determined by eight parameters, as $\Pi_\star$ remains free.

A necessary condition, to extract energy from the black hole, is to choose negative values of e_1 for the inflow solution. In this case, it is possible to inject negative energy (see Eq.(60) of Chantry et al. 2018), as long as the black hole accretes enough magnetic flux. The magnetic flux on the equator of the black hole horizon must be higher than the minimum threshold value. In dimensionless form, it writes as $\alpha_H > -1/e_1$. In Tab.(1), we give the set of input parameters used for building three inflow/outflow solutions of the meridionally self-similar model.

We show in Tab.(2) the output results of our three solutions, under minimal matching conditions Eq.(58). We give a the usual dimensionless black hole spin in unit of the gravitational radius, Ω/ω_H the isorotation frequency in unit of angular velocity on the black hole horizon, and $r_{\rm sta}/r_H$ the stagnation radius in unit of black hole horizon radius. We also give, for the three global solutions, the maximum Lorentz factor and $\xi_\star$ the effective enthalpy at the Alfvén point, both along the polar axis.

We choose the input parameters, both for the inflow and the outflow, in order to satisfy specific conditions for the solutions and to match them under the minimal conditions. We require the final outflow Lorentz factor on the axis to be higher than 10. The variation of the Lorentz factor with the magnetic flux in the inflow is negative or null on the north pole horizon. Thus, we use numerical gradient descent techniques in the parameter space (see Appendix C).

We start by building three inflow solutions with different kind of energy exchange with the black hole that satisfy our constraints. Then using the numerical descent technique, we build three outflow solutions matching, each matching one of our inflow solution. We get a discrepancy for a, Ω/ω_H and $r_{\rm sta}/r_H$ between the inflow solution (I1, I2 or I3) and the outflow solution (O1,O2 and O3 respectively) lower than 10^{-2}. The parameters are listed in Tab.(2). The numerical value of $\gamma_{\rm max,ax}$ is not infinite on the black hole horizon, along the axis. It is numerically impossible to get an inflow solution with $\gamma = +\infty$ on the horizon so we choose to have $\gamma_{\rm max,ax} > 10$. We could tune $\Pi_\star$ in the inflow to get this constrain for γ close to the horizon. As explained in Appendix A, this implies that the Π function behaviour near the horizon is close to $\ln(R - R_H)$, but at a smaller radius starts to behave as $1/(R - R_H)$. Instead of adapting the inflow $\Pi_\star$ in order to increase $\gamma_{\rm max,ax}$, we prefer to keep a degree of freedom to solve the difficulties of the matching conditions. Let us also remind that, in the outflow with high asymptotic Lorentz factor, this factor deviates slightly from its maximal value in the asymptotic regime. This is due to numerical reasons, because it is not possible to get a sufficiently precise value of $\Pi_\star$ to tune it to the non oscillating value.

To obtain the solution we also need to fix the value of the three parameters M, $B_\star$ and $\xi_\star$. The geometry and the velocity profiles of one solution are not depending on these free parameters. We set the black hole mass to $6.6\times10^9 M_\odot$, which is the value mention in Gebhardt et al. (2011) for the M87 black hole mass. This is within the range measured by the Event Horizon Telescope Collaboration, $M = 6.5\pm0.7\times10^9 M_\odot$. As discussed above, we use observational constraints to fix the magnitude of the second parameter, the magnetic field strength $B_\star$. Since the solution M1 has a stagnation radius larger than $5r_g$, we use $B(20r_g) \approx 1$G and we take $B_{\star,\rm out} \approx G^2_{\rm out}(20r_g)$G. For solutions M2 and M3 the stagnation radius is lower than $5r_g$, then we use $B(5r_g) \approx 4.9$G and we take $B_{\star,\rm out} \approx 4.9G^2_{\rm out}(5r_g)$G. We put in Tab.(3) the values of $B^{\rm in}_\star$ obtained for each solution.

Once the value of $B_\star$ is determined, the value of $\rho_\star\xi_\star$ is known from the definition of the Alfvén surface. From Eqs.(73) and (74) of Chantry et al. (2018), the effective enthalpy and the mass density fields are scaled by the factors $\xi_\star$ and $\rho_\star$, respectively. Once $\xi_\star$ is

given, both the effective enthalpy and the mass density field scaling are fixed .

We choose $\xi_\star$ for the outflow solution as in Chantry et al. (2018), such that the effective internal energy at infinity on the axis reduces to the internal energy of a gas at thermodynamic equilibrium.

Zamaninasab et al. (2014) define a scaling-law $\Phi^Z_{\rm jet} = f_Z\sqrt{\dot{M}c\left(\frac{r_s}{2}\right)^2}$ between the magnetic flux of the jet and the total disk accretion rate $\dot{M}$. They deduce from observations a value of $f_Z \sim 50$. They assume that the jet power is the result of a pure Blandford-Znajek mechanism. Thus they deduce that the black hole magnetic flux $\Phi_{\rm BH}$.

We use a similar scaling law for the black hole magnetic flux $\Phi_{\rm BH} = f\sqrt{\dot{M}_{\rm Inf}c\left(\frac{r_s}{2}\right)^2}$ and the inflow mass rate. Our scaling factor f must be larger than f_Z since the magnetic flux of the jet is only part of the one threading the black hole in the inflow zone. We choose $f \sim 150$, a value three times higher than $f_Z \sim 50$, because we choose $\dot{M}_{\rm inf}$ of order one tenth of $\dot{M}$ for the same magnetic flux $\Phi_{\rm BH}$. In our model the efficiency to create magnetic flux from the pair inflow is higher that the one deduced from standard Blandford-Znajek theory applied in the jet at 1 pc. This scaling law is used to define the value of $\xi_\star$ in the inflow.

Thus, from the model we can derive,

$$\Phi^2_{\rm BH} \approx \frac{\sqrt{\mu}\xi_\star\gamma_\star\left(1+\sqrt{1-\left(\frac{2l}{\mu}\right)^2}\right)}{|\nu|h_\star G_H^2}\dot{M}_{\rm inf}c\left(\frac{r_s}{2}\right)^2, \tag{72}$$

which leads to,

$$\xi_\star = \frac{|\nu|h_\star G_H^2}{\sqrt{\mu}\gamma_\star\left(1+\sqrt{1-a^2}\right)}f^2, \tag{73}$$

where all the quantities are evaluated in the inflow.

3.2 Field line geometry with quasi-isotropic coordinates

Fig.(5) shows the fieldline geometry of the matching solutions. We plot for each solution a zooming view of the field lines close to the environment of the black hole for the inflow, and a larger view of the outflow, including the external light cylinder. Instead of using a simple Cartesian version of the Boyer-Lindquist coordinates, or what is called pseudo-Cartesian coordinates, we opted for the use of so-called quasi-isotropic coordinates. In Chantry et al. (2020) we discussed in details their properties. This choice of coordinates presents two main advantages. First, it allows a conformal representation and therefore a correct representation of the angles. Thus the property of the orthogonal field line penetration into the horizon is correctly visualized. Secondly, these coordinates expand the representation in the black hole environment, which allows to show more details in this area.

We plot in the left panel of Fig.(5) the poloidal field geometry only for the open field lines linking the black hole horizon to infinity ($A < A_{\rm mag}$). First, our model (inflow and outflow) is deduced from an expansion to second order of the colatitude in Euler's equations. This explains why it is physically relevant close to the axis and in the region with small colatitudes. For a given second order expansion in colatitude we should quantify the deviation to the equilibrium of Euler's equations and normalize with the strongest volumic force to estimate the region of validity. This calculation is quite complicated, and we decide to examine the solutions inside of the region defined by the last open field line which contains the region of validity.

Second, we cannot use our model for the magnetospheric dead zone ($A > A_{\rm mag}$ and $r < r_{\rm mag}$). It would induce artificial source terms on the equatorial plane with $r_H < r < r_{\rm mag}$. For $r > r_{\rm mag}$ the source terms could be explained by the presence of the accretion disk but we prefer to avoid this region in our modelling.

As explained in Takahashi et al. (1990), the stagnation surface and the injection are located between the two light cylinders. All the field lines are continuous but not C^1 at the stagnation surface. On this surface there is a kink in the fieldlines related to the surface current density. Two different trends are observed for the the expansion factor of the streamlines F. In the matching solutions M1 and M2, the field lines are flaring more in the starting region of the inflow than at the base of the outflow $F_{\rm sta,in} \geq F_{\rm sta,out}$. The situation is the opposite for the M3 solution $F_{\rm sta,in} \leq F_{\rm sta,out}$. The corotation surface location appears below the stagnation surface for the solution M1 and above for the solutions M2 and M3. The larger is Ω, the smaller is the mean radius of the corotation surface.

We also observe different sizes for the inflow. The size of the last open line in the magnetosphere is significantly larger for the M2 solution. The size of the magnetosphere of the M2 solution reaches on the equatorial plane an approximate value of $75r_g$. This is slightly larger than the Alfvén radius of the outflow. While for the other solutions, the magnetosphere is located inside the Alfvén surface and reaches approximately $40r_g$ for solution M1 and $8r_g$ for solution M3, on the equatorial plane. The open lines represent 14% of the total magnetic flux passing through the black hole horizon for M1, less than 1% for M2 and around 8, 5% for M3.

3.3 Interface between inflow and outflow

The interface corresponds to the region with poloidal velocities close to zero. This region, in our model, is the one where the flow is loaded via creation of pairs or any other mechanism. In fact, the matching of the inflow and the outflow solutions puts some constraints on the loading terms, as detailed in Subsec. (2.4). Once the matching of the two solutions is obtained the injection or loading terms can be calculated. First, we discuss the surface charge density and the toroidal current flux sources we obtain at this interface. Then we explain how we inject mass, angular momentum and energy.

3.3.1 Electromagnetic sources on the stagnation surface

The electromagnetic sources on the stagnation surface are fully determined by σ_e and $J^{\hat{\theta}}_\sigma$ because the ratio of σ_e on $J^{\hat{\varphi}}_\sigma$ is given by Eq.(53),

$$\frac{\sigma_e c}{J^{\hat{\varphi}}} = -\frac{\varpi\,(\Omega-\omega)}{hc} = -x, \tag{74}$$

where x is the dimensionless cylindrical radius.

First, let us note that the sign of σ_e is the same as the one of $-(F_{\rm sta,out}-F_{\rm sta,in})(\Omega-\omega)_{\rm sta}$. We plot σ_e and $J^{\hat{\theta}}$ on Fig.(6). For the M1 solution, the corotation surface is located below the stagnation surface where $\Omega > \omega$. We observe that $F_{\rm sta,out} < F_{\rm sta,in}$ and the flaring of the poloidal field lines increases where they cross the stagnation surface (see Fig.(5)). These two facts explain the positive sign of σ_e and the negative one of $J^{\hat{\varphi}}$. For M2, the corotation surface is above the stagnation surface. The same increase of the magnetic field line flaring occurs at the crossing of the stagnation surface implying $\sigma_e < 0$. For the last solution M3, the corotation surface is also above

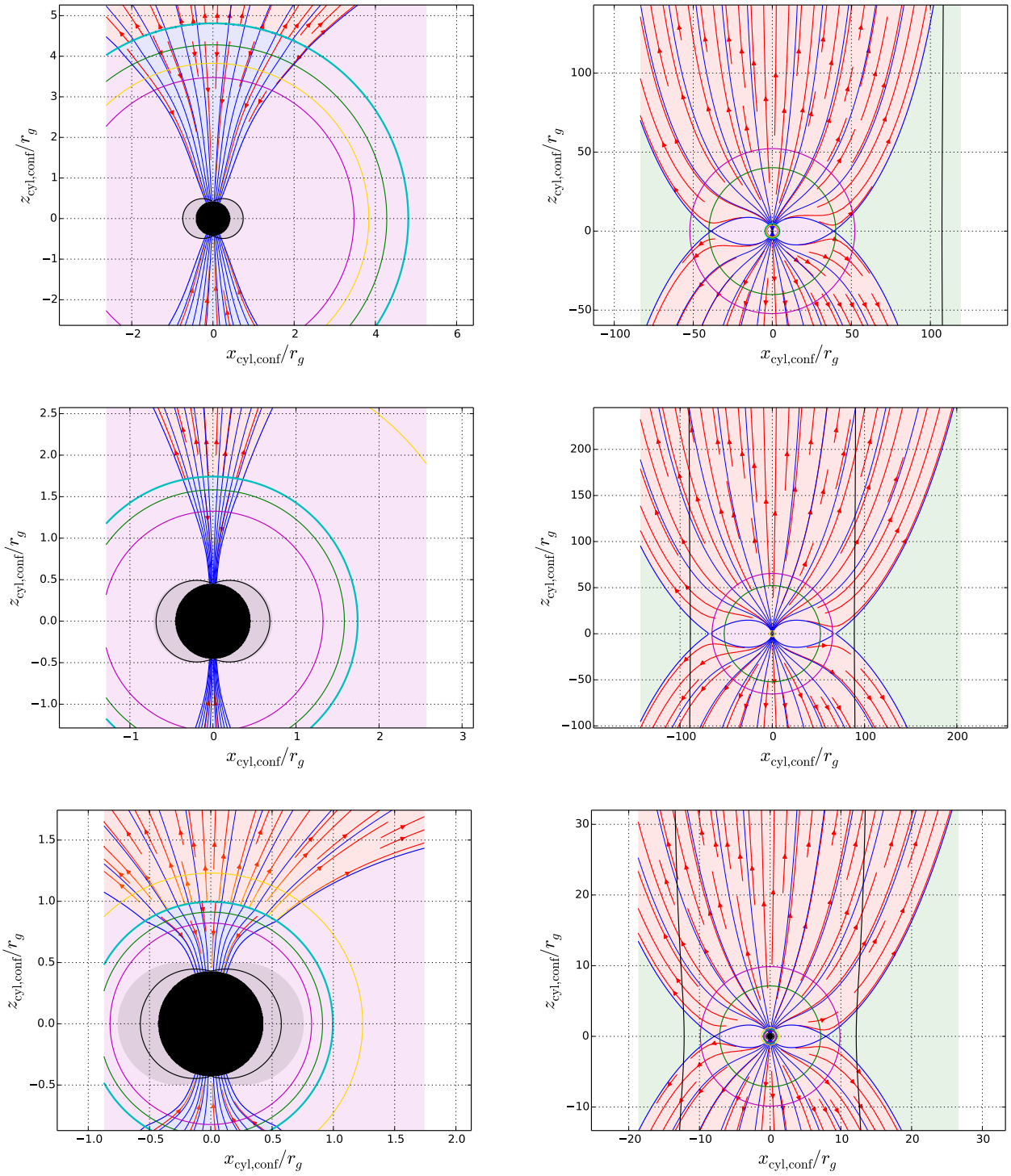

Figure 5. Poloidal field lines on two different scales for the three solutions (M1 top solution, M2 middle one and M3 bottom one). On the left we zoom inside the stagnation radius, and on the right the scale encloses the outer light cylinder radius. The red arrows represent the mass flux $\rho_0 h\gamma \mathbf{V}_P$ and the thin blue lines, the poloidal magnetic field lines. The thick blue line marks the last open magnetic field line of the flow connected to the black hole. The yellow line represents the position of the corotation surface where $\Omega = \omega$. The cyan circle corresponds to the stagnation surface, the green ones to the slow-magnetosonic surfaces and the magenta ones to the Alfvén surfaces. The light cylinder surfaces are marked both in black. The magnetosphere is represented in purple, the open line flow region in light red. The region where we expect the disk wind is in green, the ergoregion in light gray and the inner horizon region in black. We used quasi-isotropic coordinates to plot this figure.

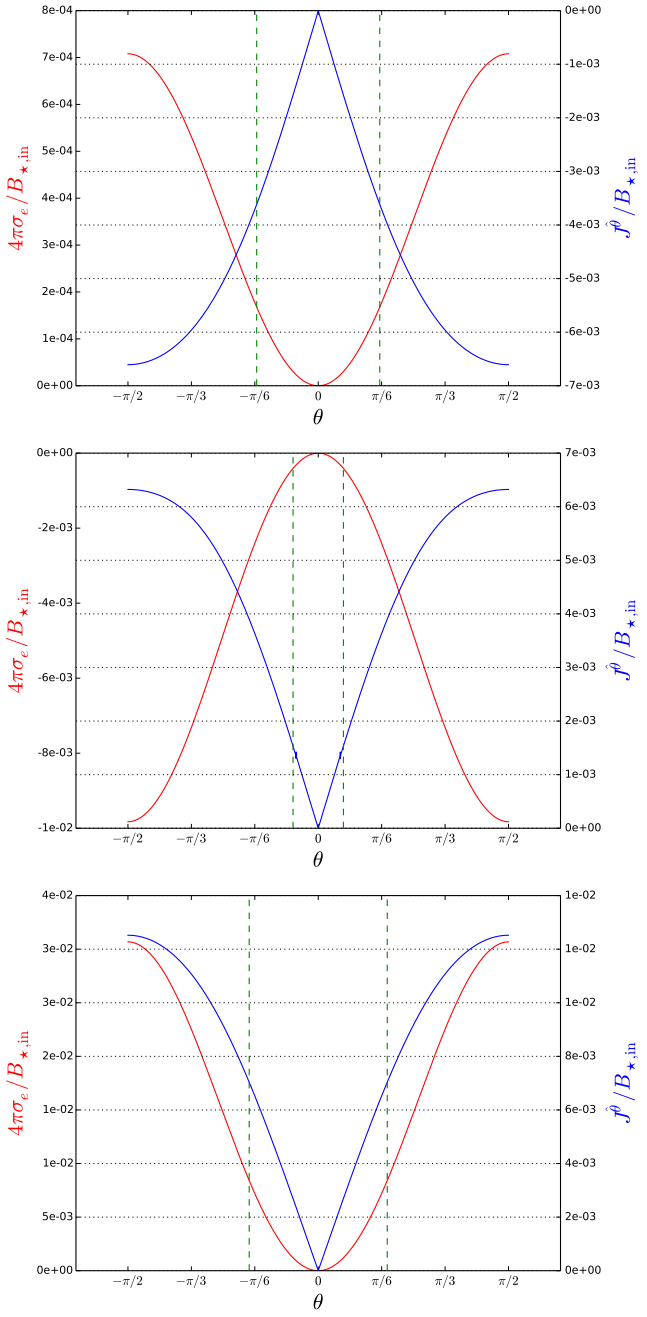

Figure 6. Surface electromagnetic sources as a function of the colatitude for the different solutions. The top solution is M1, the middle one M2 and the bottom one is M3. In red, the surface density of charge is plotted as a function of the colatitude and, in blue, we plot the dimensionless toroidal surface current. The vertical dotted green lines represent the colatitude on the stagnation surface of the last open poloidal magnetic field lines.

the stagnation surface but the flaring of the magnetic poloidal lines decreases across the stagnation surface implying $F_{\rm sta,out} > F_{\rm sta,in}$ and $\sigma_e > 0$.

As it can be seen on Fig.(6), $J^{\hat{\theta}}_{\sigma}$ is negative for M1 and positive for M2 et M3. The sign of $J^{\hat{\theta}}_{\sigma}$ is determined by the direction of the shift at the stagnation surface of the current line with $I = $ cst (see Fig.(4) where $J^{\hat{\theta}}_{\sigma} < 0$). A positive surface current $J^{\hat{\theta}}_{\sigma}$ implies a decreasing of the current I across the stagnation surface (see Eq.(56) and then a increasing of the Poynting flux $\propto -I\Omega$.

3.3.2 *Loading terms*

The loading terms bring mass, angular momentum and energy to the MHD fields and to the black hole. Here these quantities are the result of the minimal matching conditions given by Eq.(58).

The injection terms are proportional to the scaling factor Eq.(68) determined by the value of $B^{\rm in}_{\star}$. We already gave an estimation of the magnetic field along the polar axis at the Alfvén radius for the M87 black hole (see Tab.(3)). We found $B_{\star,\rm out} \approx G^2_{\rm out}(20r_g)$G for M1 and $B_{\star,\rm out} \approx 4.9G^2_{\rm out}(5r_g)$G for M2 and M3. From this value, we can estimate, for the inflow solution, the alfvénic magnetic field on the axis $B_{\star,\rm in}$ and the magnetic field on the black hole horizon B_H. For the three solutions we get a magnetic field on the black hole horizon between 300 and 600 Gauss. Eq.(68) allows us to estimate, for the inflow solution, the constant values for the mass, energy and angular momentum injected per unit time and dimensionless magnetic flux, α. These quantities have been calculated for the three global inflow/outflow solutions as shown in Tab.(3).

Now, we can compare the physical quantities for the three matching solutions with the ones obtained by other works. They depend on the considered phenomena and injection models. For example, let us evaluate the amount of mass that can be injected via pair creation from hard photons emitted by the accretion disk. Following Levinson & Segev (2017), the injection rate per unit volume is estimated as $\sigma_{\gamma\gamma} n^2_\gamma c$, where n_γ is the density of hard photons with an energy ϵ_γ ($\epsilon_\gamma > 1\,$MeV $\approx 2m_e c^2$). We use the Thomson cross section $\sigma_{\gamma\gamma} \approx 6,6\times10^{-25}\,$cm^2 for estimating the cross section of pair production. Now let introduce the dimensionless radius of the hottest part of the disk $R_\gamma = r_\gamma/r_g$, the dimensionless mass $m = M/M_\odot$, and the dimensionless luminosity $\ell_\gamma = L_\gamma/L_{\rm Edd}$, where L_γ is the luminosity of hard photons and $L_{\rm Edd}$ the Eddington luminosity. Then the luminosity, coming essentially from the disk, is related to the photon density $L_\gamma = 4\pi r^2_\gamma n_\gamma c\epsilon_\gamma$, which leads to,

$$n_\gamma \approx 10^{22}\frac{\ell_\gamma}{mR^2_\gamma}\,\text{cm}^{-3}\,. \tag{75}$$

Then we estimate the mass injection rate,

$$\dot{M}_{\rm Inj} \approx 1,6\times10^{20}\frac{\ell^2_\gamma m}{R^4_\gamma}\,\text{g.s}^{-1}\,. \tag{76}$$

Using values of luminosity mentioned in Prieto et al. (2016) for M87, we get $\ell_\gamma \sim 10^{-7}-10^{-4}$. Taking $m \approx 6\times10^9$ and $R_\gamma \sim 10-10^2$, see Event Horizon Telescope Collaboration 2019 for the dimension of the emission ring. Note that Event Horizon Telescope Collaboration (2021) have shown, using their library of disc models, that the inner radius of the disk lays within $\approx 10-20r_g$. From these estimates, we get $\dot{M}_{\rm Inj} = 10^8 - 10^{20}\,$g.s^{-1}. The factor R^{-4}_γ makes this estimate extremely sensitive to the value of R_γ. Calculations based on Pu et al. (2015), with different matching conditions, lead to similar conclusions.

Nevertheless, many works (Levinson & Rieger 2011, Hirotani et al. 2016) show that this injection does not allow to reach the Goldreich-Julian density necessary for the screening of the transverse electric field. In this case, spark gap may form (Levinson & Segev 2017) along the magnetic field. The electric acceleration combined with Compton and Inverse Compton processes allow an additional source of pair production. This mechanism leads to mass injection in the lower range, up to $10^{11}-10^{12}g.s^{-1}$, which is a bit low for our models.

Solution	$B_\star^{\rm in}$ ($\rm cm^{-1/2}.g^{1/2}.s^{-1}$)	B_H ($\rm cm^{-1/2}.g^{1/2}.s^{-1}$)	$\dot{M}^\star_{\rm Inj}$ ($\rm g.s^{-1}$)	$\dot{J}^\star_{\rm Inj}$ ($\rm g.cm^2.s^{-1}$)	$\dot{E}^\star_{\rm Inj}$ ($\rm erg.s^{-1}$)
M1	$8,7\times10^1$	$5,84\times10^2$	1.21×10^{23}	3.56×10^{48}	1.09×10^{44}
M2	$8,2\times10^1$	4.7×10^2	$1,1\times10^{23}$	3.2×10^{48}	9.8×10^{43}
M3	$1,3\times10^2$	$3,19\times10^2$	2.62×10^{23}	7.7×10^{48}	2.36×10^{44}

Table 3. In the first and second columns we give the estimated values of the magnetic field on the inflow Alfvénic point and on the black hole horizon, respectively. In the three last columns we plot the constant values for the mass, angular momentum, and energy per infinitesimal intervals of time and of dimensionless magnetic flux for a black hole mass equal to the one of M87. Each line corresponds to one of the three inflow/outflow solutions of the meridional self-similar model. We use $B(20r_g) \approx 1$G to calculate $B_\star^{\rm out}$ for the solution M1 since the stagnation radius is around $5r_g$ and $B(5r_g) \approx 4.9$G for the two other solutions, M2 and M3.

However, recent works with particle-in-cell simulations (e.g. Crinquand et al. (2021)) explore the dynamics of the formation of such gap and the role of magnetic reconnection allowing to visualise the location of pair formation. Their conclusions tend to suggest that gaps are intermittent. Thus, we use more recent radiative GRMHD simulations to give a more precise estimation of the mass injection rate (Yao et al. 2021). Fig.(10) of this publication gives an average in time of the pair production rate as a function of the radial distance in a region close of the axis. Assuming spherical symmetry and the value mentioned in this plot for the MAD W18 disk model, we can estimate the total injected mass. We obtain a total amount of $2.5m_9^3\times10^{14}\,\rm g.s^{-1}$, where the black hole mass is $m_9\times10^9 M_\odot$. For M87, it gives a total injected mass $\approx 8\times10^{16}\,\rm g.s^{-1}$. This amount is sufficient to screen the electric field and avoid the formation of the spark gap along the axis region close to the black hole.

Globus & Levinson (2013) explored the injected critical mass for which no extraction occurs. For a cold flow and a magnetic flux $\approx 10^{27}\,\rm G.cm^2$, which crosses the black hole, the mass flux limit find by the authors depends from the value of a and θ but is around $10^{25}-10^{30}\,\rm g.s^{-1}$.

In Tab.(4), we put the minimum, the maximum and the mean value of the injected mass per unit time and per unit dimensionless magnetic flux. After integration for $A < A_{\rm mag}$, we obtained the total injected mass and the injected mass in the inflow per unit time. These values are put in the Tab.(4). In the first column we indicate the dimensionless magnetic flux for the last open magnetic field line of the outflow. Note that the values of $\alpha_{\rm Mag}$ are similar for the three global solutions, despite the large variation of the sizes of the magnetosphere on the equatorial axis.

In Tab.(4) the total injected mass is, for M2 and M3 in the upper range of the estimation based on the EHT emission ring size. We get a larger value only for solution M1. Globally, we obtain an injected mass which is two to four orders of magnitude higher than the one obtained by Yao et al. (2021). For the M1 and M3 solutions, most of the injected mass per unit time is flowing outward, quantitatively 80% for M1 and 66% for M3. Conversely, for the M2 solution, only 6% of the total injected mass per unit time is flowing outward.

In Fig.(7) we plot in blue the injected angular momentum rate per unit dimensionless magnetic flux. Its sign is positive for solutions M1 and M3 and negative for solution M2. The total amount of angular momentum rate per unit time is equal to $(10^{-3}-10^{-2})J^\star_{\rm inj}$. We also plot the injected power per unit magnetic flux. This quantity decreases slowly with the magnetic flux due to the negative value of e_1 for the inflow solutions. The order of magnitude of the total amount of injected energy is $5.4\times10^0 E^\star_{\rm inj}$ for M1, $6.3\times10^{-2}E^\star_{\rm inj}$ for M2 and $10^{-1}E^\star_{\rm inj}$ for M3.

3.4 Kinetic and dynamics of the inflow

Fig.(8) shows the fluid celerity $\gamma\beta$ measured by the ZAMO observer along the polar axis. The Lorentz factor reaches relatively high values $(10-25)$ as expected. In fact the parameters could be tuned in order to have $\gamma \longrightarrow +\infty$ and to smooth the pressure function Π behaviour close to the black hole horizon.

Consider the forces acting on the inflow. The situation is quite similar for the different solutions. We plot in Fig.(9) the transverse and longitudinal forces for a field line close to the axis for solution M2.

The upper part of Fig.(9) represents the transverse forces for the M2 inflow solution. Positive values correspond to the collimating forces. Near the stagnation surface the gravitational force is the main decollimating force, which is in quasi-equilibrium with the sum of the magnetic forces (i.e. basically the magnetic poloidal pressure and the magnetic tension) and the pressure gradient. Near the black hole the gravitational and electrical forces (decollimating) are in equilibrium with the magnetic forces, i.e. essentially the magnetic poloidal tension, plus the poloidal advection force.

The bottom part of Fig.(9) corresponds to the longitudinal forces. Negative (positive) values means that the forces are directed towards (outwards) the black hole center. The main force driving the flow is gravity. The pressure also plays an important role in the part of the flow where the acceleration decreases the pressure, i.e. by a cavitation effect. The main opposite force is due to the fluid inertia, the advection term, plus the pressure at the stagnation layer and on the black hole horizon.

3.5 Energy exchange between the black hole and the MHD fields

We plot on Fig.(10) Noether's energy and angular momentum exchange between the MHD inflow and the black hole. The colatitude of the open field lines at the black hole horizon is plotted by green dotted points. We have drawn Noether's energy and the angular momentum exchange beyond this angle because we were interested for getting the different energy fluxes beyond it. Furthermore the fluxes on the black hole are determined by the MHD fields on the horizon. In terms of the outflow model parameters $(\lambda,\kappa,\delta,\nu,\mu,l,e_1)$, the matching conditions bring three effective constraints on model parameter. Then we expect that for a fixed outflow, which satisfies the Eq.(58), there is a $7-3=4$ dimensional submanifold of the outflow parameter space of matching solutions. Because we impose that the last inflow field line corresponds to the last open outflow field line, the colatitude of this last field line on the horizon depends also of the chosen outflow solution.

Angular momentum is extracted from the black hole for each inflow/outflow solution for the whole range of colatitude except on

Solution	$\alpha_{\rm Mag}$	$\left.\frac{1}{\dot{M}^\star_{\rm Inj}}\frac{{\rm d}^2 M_{\rm Inj}}{{\rm d}t{\rm d}\alpha}\right\vert_{\rm Min}$	$\left.\frac{1}{\dot{M}^\star_{\rm Inj}}\frac{{\rm d}^2 M_{\rm Inj}}{{\rm d}t{\rm d}\alpha}\right\vert_{\rm Max}$	$\langle\frac{1}{\dot{M}^\star_{\rm Inj}}\frac{{\rm d}^2 M_{\rm Inj}}{{\rm d}t{\rm d}\alpha}\rangle$	$\dot{M}^{\rm tot}_{\rm Inj}$	$\dot{M}^{\rm tot}_{\rm Inj,in}$
M1	0.95	8.2×10^{-3}	1.12×10^{-2}	9.7×10^{-3}	1.1×10^{21} g.s^{-1}	2.4×10^{20} g.s^{-1}
M2	0.99	8.63×10^{-5}	8.87×10^{-5}	8.8×10^{-5}	9.5×10^{18} g.s^{-1}	$8,95\times10^{18}$ g.s^{-1}
M3	0.98	8.25×10^{-4}	1.12×10^{-3}	9.7×10^{-4}	1.3×10^{20} g.s^{-1}	$4,3\times10^{19}$ g.s^{-1}

Table 4. The first column indicates the dimensionless magnetic flux for the last open magnetic field line, which marks the limit of the magnetosphere in the outflow. In the second, third and fourth columns, we give the minimum, the maximum and the mean value of the mass injected per unit time and unit dimensionless magnetic flux, at the stagnation surface, for $A < A_{\rm mag}$, respectively. The fifth and sixth columns five give the total mass injected and the mass injected in the inflow per unit time at the stagnation surface for $A < A_{\rm mag}$, respectively. Each line corresponds to one of the three inflow/outflow solutions.

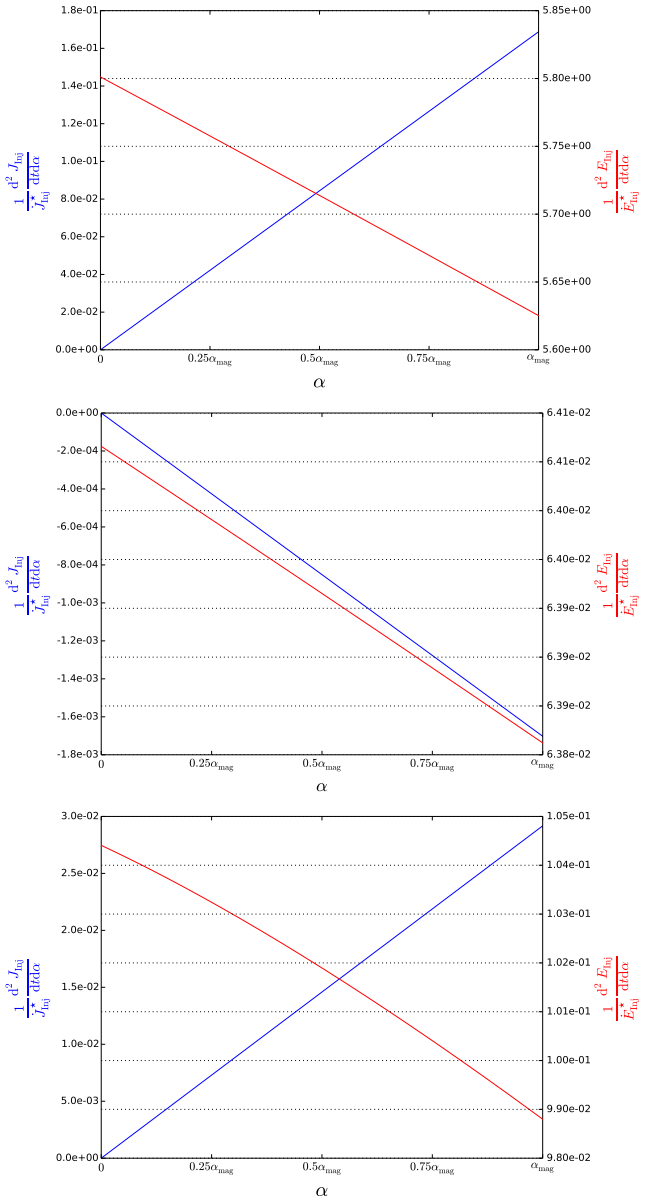

Figure 7. Injected angular momentum and energy at the interface per unit time and dimensionless magnetic flux as a function of the magnetic flux for the different solutions. On top, we plot M1 ($\alpha_{\rm Mag}\approx0.95$), in the middle M2 ($\alpha_{\rm Mag}\approx0.99$) and at the bottom M3 ($\alpha_{\rm Mag}\approx0.98$). The angular momentum is plotted in blue. It is divided by its scaling value $J^\star_{\rm inj}$. The energy is plotted in red and divided by its scaling value $E^\star_{\rm inj}$.

the axis. If we look at the Fig.(10), the amount of extracted angular momentum in dimensionless units has a maximum which varies by one order of magnitude from solution to solution. Nevertheless taking into account the constant values in Tab.(3), we calculate the extracted angular momentum integrated over the open field lines and on the whole black hole horizon. These values are mentioned in columns two and three of Tab.(5). On the open field lines, there is one order of magnitude difference for the extracted angular momentum at the black hole horizon, $\dot{J}_{\rm H,open}$, between M3 and M1 solutions. But on the whole black hole horizon, M2 extracts more efficiently angular momentum than the two other solutions. This result is due to the very small extension of the open field line region on the black hole horizon for the M2 solution. For open field lines, we note that the extracted angular momentum on the black hole horizon is of the same order of magnitude as the injected angular momentum at the stagnation surface.

None of our solutions are capable of having a positive global extraction of Noether energy along the open magnetic field lines. This is due to the fact that, close to the axis, the inertial energy (see Eq.(42)) is dominant. This energy is negative on the black hole horizon. For the global solutions M2 and M3, there is a positive extraction of energy but only at colatitudes close to the equatorial plane. We tried with our gradient descent method (see Sec. C) to tune the inflow parameters in order to decrease the angle where the global extraction starts. We need further studies to see if solutions exist with a global extraction of Noether's energy occurring on some of the opening magnetic field lines. However, this may be an intrinsic limitation of our model, due to the self-similarity.

As presented above, the Noether energy flux of the MHD fields can be decomposed in three main terms, the inertial energy term, $\Phi_M = \Psi_A h\gamma\xi c^2$ strictly negative on the black hole horizon, the Lense-Thirring term, $\Phi_{\rm LT} = \Psi_A\gamma\xi\varpi\omega V^{\hat{\varphi}}$, and the Poynting flux, $\Phi_{\rm EM} = -h\varpi\Omega B^{\hat{\varphi}}$. In Fig.(11), we plot these fluxes per unit colatitude. In the first solution M1, the energy flux is fully dominated by the fluid one and the Poynting flux is extremely small. This could be explained by the value of Ω/ω_H (see Tab.(2)). The Lense-Thirring flux is negative which means that the fluid falls into the hole with positive $V^{\hat{\varphi}}$. In the second solution M2, the Poynting flux is still small, but outside of the open field lines the Lense-Thirring flux is positive. For biggest colatitudes, the Noether energy flux of the fluid, the sum of $\Phi_{\rm LT}$ and Φ_M), become positive, which means that the Penrose fluid process is efficient. In the last solution M3, we get almost the maximum value of 0.5 for Ω/ω_H. The Poynting flux starts to be important even in the open field line region.

Blandford & Znajek (1977) derived the Poynting flux, using the boundary conditions given by Znajek (1977) close to the black hole horizon in Carter tetrad. In our model these boundaries conditions are induce by the ideal conduction Eq.(16) if the poloidal velocity in the ZAMO frame is equal to the speed of light. If we use this condition

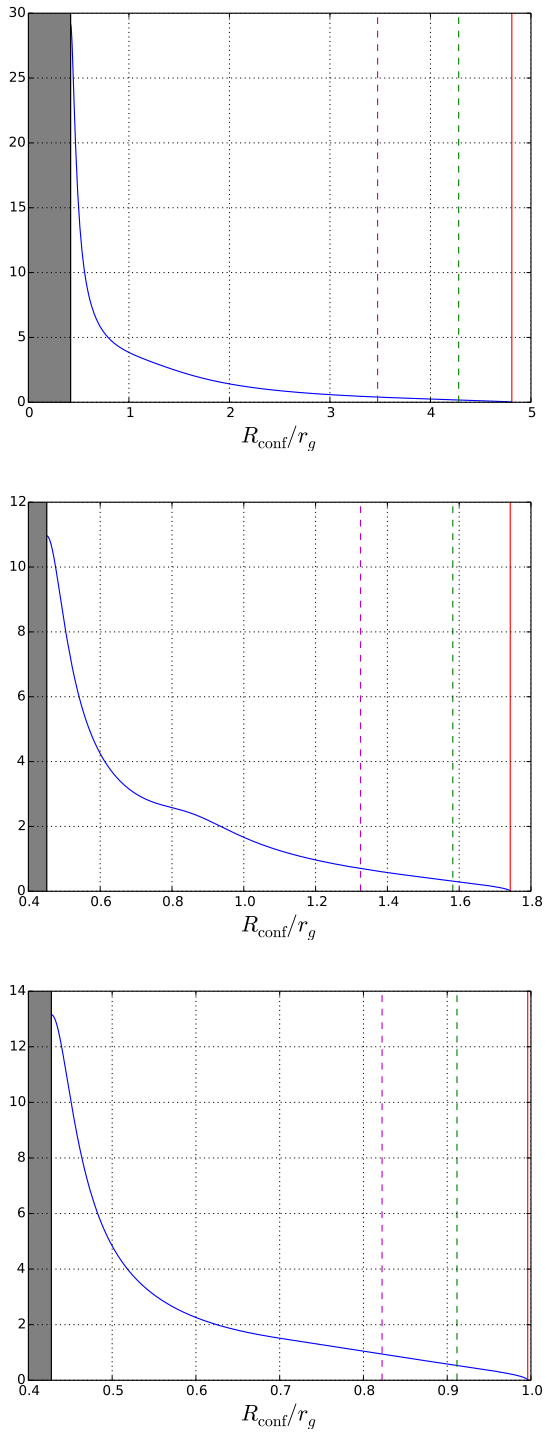

Figure 8. Plot of the celerity $\beta\gamma$ of the inflow plasma along the axis as a function of the quasi-isotropic radial distance for the different solutions, M1 on top, M2 in the middle and M3, bottom. The vertical lines correspond to the different critical surfaces, namely, the Alfvén one in dotted magenta,the slow-magnetosonic one in dotted green and the stagnation surface in red. The grey shaded area corresponds to the inner part of the black hole horizon.

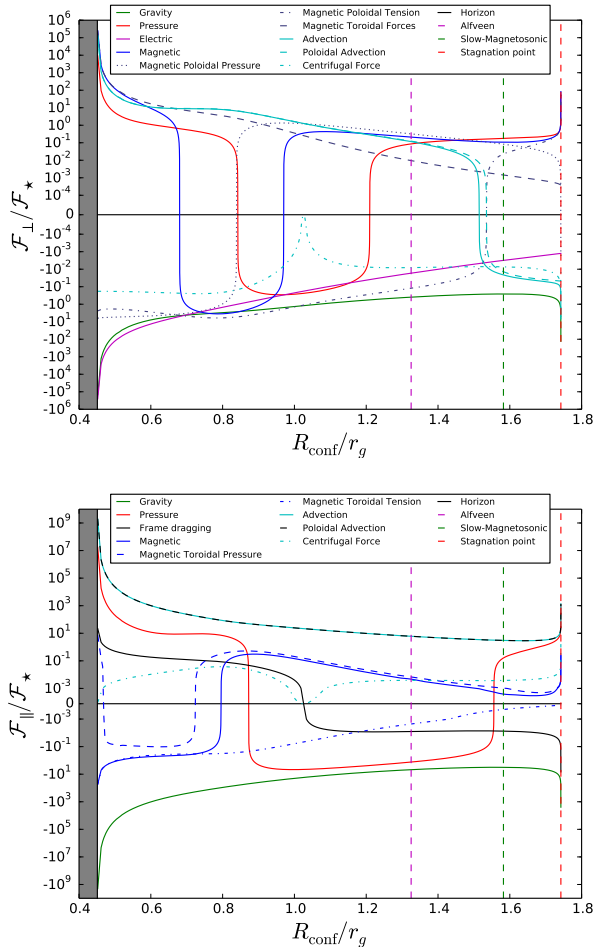

Figure 9. For the inflow of solution M2, we plot the transverse forces as function of the quasi-isotropic radial distance, on top, with a positive value for forces directed inward the flux tube. We plot the longitudinal forces, bottom, with a positive value for decelerating forces. The grey shaded area corresponds to the inner part of the black hole horizon.

in ZAMO tetrad, we also get $B^{\hat{\varphi}} + E^{\hat{\theta}} = 0$ on the horizon. In our model, at first order in colatitude, the fluid enter in the horizon with $V^{\hat{\theta}} = V^{\hat{\varphi}} = 0$ (see Chantry et al. (2018)). If we tune the parameter such that $V^{\hat{r}} = -c$ on the horizon pole this condition is immediately satisfied to order one with colatitude, as a consequence of infinite conductivity. We find for the Poynting power extracted from the black hole between the colatitudes 0 and θ,

$$\begin{aligned}\dot{E}^{\rm Poy}_{\rm H}(\theta) &= \int_0^\theta h\varpi\Omega E^{\hat{\theta}}\frac{dA}{d\theta}d\theta \\ &= 4\frac{\Omega}{\omega_H}\left(1-\frac{\Omega}{\omega_H}\right)\frac{c\Phi^2_{\rm BH}}{128\pi^2 r_g^2}\frac{a^2}{1+\sqrt{1-a^2}-a^2/2} \\ &\quad \int_0^\theta \frac{\sin\theta}{1-\frac{a^2}{2\left(1+\sqrt{1-a^2}\right)}\sin^2\theta}\left(\frac{d}{d\theta}\frac{A}{A_H}\right)^2 d\theta\,, \end{aligned} \tag{77}$$

where $2\pi A_H = \Phi_{\rm BH}$ and A is evaluated on the horizon and a function of θ only. The Poynting power is then determined by Ω and the magnetic flux function A on the black hole horizon. No fluid quantity is entering in this expression. It means that we obtain a Poynting power

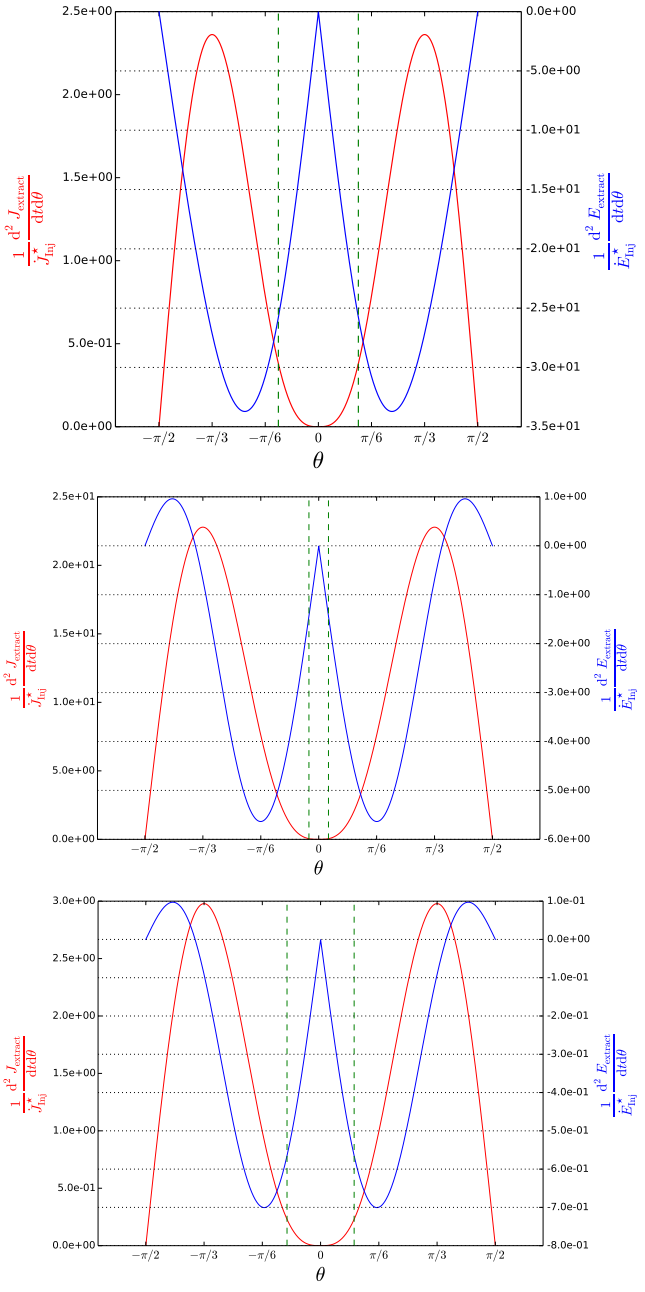

Figure 10. Global balance on the black hole horizon of the Noether energy and angular momentum for the three solutions, M1 on top, M2 middle and M3 bottom. In red, the dimensionless extracted Noether angular momentum per unit colatitude and time. In blue, the dimensionless extracted Noether energy per infinite intervals of colatitude and time. The dotted green lines indicate the colatitude of the last magnetospheric field line at the horizon radius.

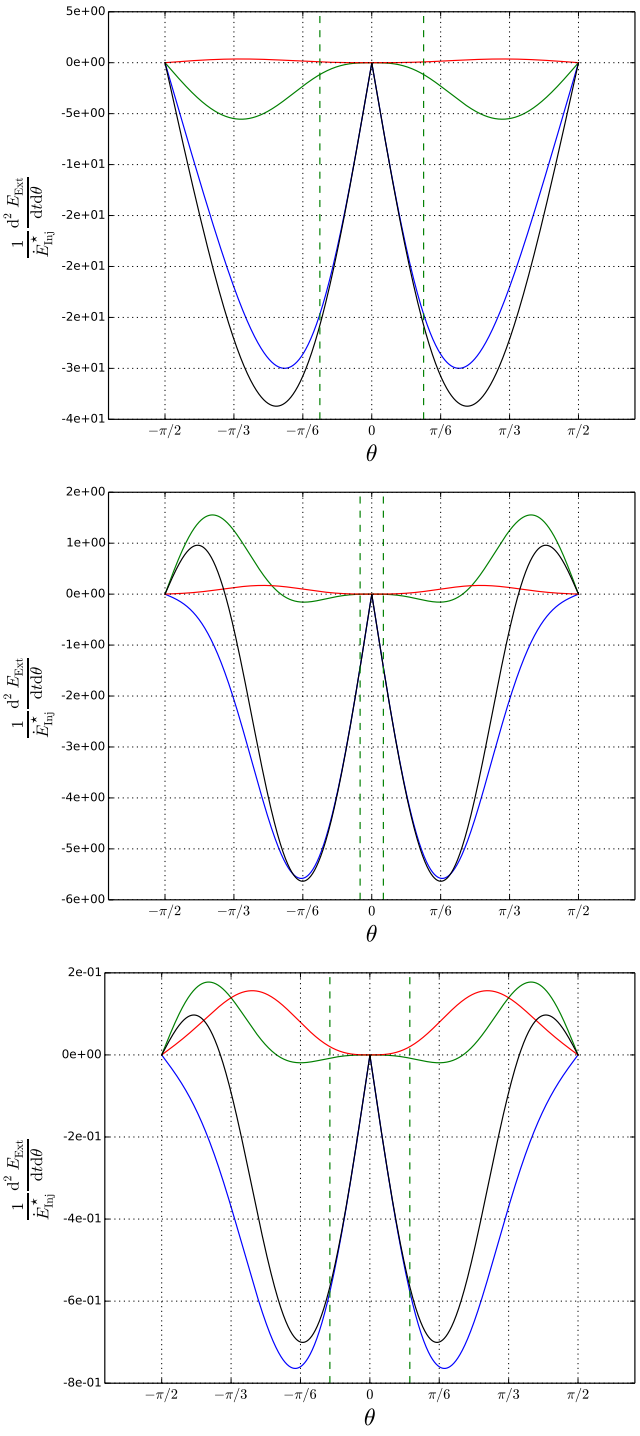

Figure 11. Noether energy flux component per unit colatitude flowing across black hole horizon in function of the colatitude for the three solutions (M1 on top, M2, middle and M3, bottom). In red the Poynting flux, in blue the inertial flux, in green the Lense-Thirring flux and in black the total MHD flux. As before the dotted green lines indicates the colatitude of magnetosphere field line at horizon radius.

similar to the one obtained in the free-force assumption (Blandford & Znajek 1977, see also Eq.(26) of Globus & Levinson 2013).

3.6 Outflow energy and angular momentum sources

Now we can compare the sources of injected angular momentum, in dimensionless units, by pair injection in the stagnation surface and by the black hole. In Tab.(5), we note $\dot{J}_{\rm H,open}$ the angular momentum flux extracted from the black hole and $\dot{J}_{\rm inj,open}$ the angular momen-

tum flux injected by pairs creation. Both fluxes are limited to the inner region of open magnetic field lines. For the M1 and M3 solutions, the angular momentum injected by pair creation, $\dot{J}_{\rm inj,open}$, is of the same order as the angular momentum extracted from the black hole, $\dot{J}_{\rm H,open}$. However note that for M2 the pair creation causes an absorption of angular momentum, $\dot{J}_{\rm inj,open} < 0$, two orders lower than the injected angular momentum in M1 and M3. This is equivalent to say that the total angular momentum flux transported in the open magnetic field region of the inflow is larger than the one in the outflow.

In Tab.(5), $\dot{J}_{\rm H,tot}$ is the total amount of angular momentum extracted from the black hole. This total amount is larger than the angular momentum extracted into the inner region bounded by the open field lines. This is partly due to the fact that the colatitude of the last open magnetic field line is quite small on the black hole horizon, namely, $\theta_{\rm open,H} = 0.125\pi$ for M1, 0.03π for M2, and 0.10π for M3. Note that the ratio between the extracted angular momentum rate for the total and the inner regions is much higher for the M2 solution. On the inner region, the value of $\dot{J}_{\rm H,open}$ is of the same order for M1 and M3 solutions, while there is a variation for $\dot{J}_{\rm H,tot}$ between solutions M2 and M3. Changes are due to the variation of $\theta_{\rm open,H}$ but also to the changes in the magnetic field and the stagnation radius between the three solutions.

In Tab.(5) we plot the injected power by the pairs into the inner region $\dot{E}_{\rm inj,open}$, and the power extracted from the black hole into the inner region $\dot{E}_{\rm H,open}$. In order to quantify the weight of the Poynting flux in the energetic balance, we also list the extracted Poynting power into the inner region $\dot{E}^{\rm Poy}_{\rm H,open}$. We also gives the total power $\dot{E}_{\rm H,tot}$, the total Poynting power extracted from the black hole $\dot{E}^{\rm Poy}_{\rm H,tot}$. In Tab.(5) the last column is the outflow total power.

If most of the injected energy flux is going down in the inflow, we already remarked that most of the mass is moving outwards for the M1 and M3 solutions. Nevertheless the analysis in terms of mass is depending on the $\xi_\star$ value. This is a free parameter which does not change the analytical solution. This value for the inflow depends on the choice of the ratio between the inflow mass rate and the black hole magnetic flux. $\xi_\star$ of the outflow is given by the choice of P_0 (see Eqs. 54 & discussion in sub-section 5.2 of Chantry et al. (2018)).

In the inner region, the solutions present a negligible Poynting power $\dot{E}^{\rm Poy}_{\rm H,open}$ in comparison to the power extracted from the black hole $\dot{E}_{\rm H,open}$. I3 inflow solution has been optimised to reach the canonical value of $\Omega/\omega_{\rm H} = 1/2$ and the ratio between the Poynting power $\dot{E}^{\rm Poy}_{\rm H,open}$ and $\dot{E}_{\rm H,open}$ is at least one order of magnitude higher than for the two other solutions. The size of the M2 magnetosphere leads to a small opening angle of the last open field lines at the black hole horizon and then we get a small value of extracted Poynting power on the inner region for the M2 solution.

On the whole black hole horizon, the ratio between the extracted Poynting power and the total power is again higher for M3 solution. The MHD power of outflow jets corresponds to the range of the power transition between FR1 and FR2 galaxies as mentioned in Massaglia et al. (2019). Searching for different outflows which match the same inflow could be done to increase or decrease the outflow jet power.

As explained above in subsec.(3.3.1), the pairs are contributing to the Poynting flux of the outflow via the surface current $J^{\hat{\theta}}_{\sigma}$. For the M3 solution, inside the open field lines, the Poynting power at the base of the outflow is around 5.4×10^{41} erg.s^{-1} while it is around 1.2×10^{41} erg.s^{-1} below the stagnation radius in the inflow. Thus, the contribution to the Poynting power from $J^{\hat{\theta}}_{\sigma}$, created by pairs, is of the same order as the the Poynting power extracted from the black hole at the horizon.

4 DISCUSSION

Near the axis, the energy fluxes have different behaviours. The Poynting flux $\Phi_{\rm EM}$ is proportional to ϖ^2 and the fluid energy flux $\Phi_{\rm FL}$ has a non-zero constant term in its ϖ expansion. Then around the axis the fluid energy flux will be the dominant term. Furthermore, it is difficult to increase the Poynting flux relatively to the fluid energy flux. This can be explained by the equality at the Alfvén point on the axis,

$$\frac{B^2_\star}{4\pi} = \rho_\star \xi_\star \gamma^2_\star V^2_\star, \tag{78}$$

which links the typical energy of the magnetic field and the typical energy of the fluid.

In our model to increase the ratio between the Poynting and fluid energy fluxes, one way is to increase the speed on the Alfvén point and the factor $\gamma^2_\star \frac{V^2_\star}{c^2} = \frac{\mu/\nu^2}{1-\mu/\nu^2}$. For the inflow, it leads to a decreasing of the inflow Alfvén radius and then to the stagnation surface. However for small values of the stagnation radius, it is more difficult to match an outflow solution.

Eq.(77) shows that the extracted Poynting flux depends strongly on a. Increasing the Poynting flux of the M3 solution can be achieved by an increase of the black hole spin, keeping the ratio Ω/ω_H equals to $1/2$.

For the three solutions (Tab.5), most of the injected energy flux $\dot{E}_{\rm inj,open}$ goes to the inflow $\dot{E}_{\rm H,open}$ and only ten percent is injected in the outflow $\dot{E}_{\rm out,open}$. This flux is eventually absorbed by the black hole since $\dot{E}_{\rm H,open}$ is negative. Part of this energy flux is given back by the black hole into a positive Poynting flux (see Fig. 11). In a further study, we aim at searching for solutions that could extract energy from the black hole. There may be a way to optimize the eight parameters of the inflow. The first step would be to get less flaring of the inflow flux tubes in order to increase the size of opening magnetic field line region on the horizon. It is equivalent to have the last open magnetic line connected to the black hole starting at a larger colatitude. Second, we should increase the parameter ratio involved in Eq.(78) without reducing to much the radius of the stagnation, in order to increase the magnetisation and then the ratio of the Poynting flux to the fluid power.

Solving the Bernoulli equation, Globus & Levinson (2013, 2014) and also Pu et al. (2015) have developed models with a fixed geometry, obtaining double flow. The pair creation zone is either a thin layer as in our model either a volumetric injection. Despite the assumption of a radial geometry, which is a limitation of the model, Globus & Levinson (2013) use the particle source q_n (that we note k_n in the present publication) as a parameter. Above a given threshold for particle injection, the total energy flux cannot be extracted any longer. This threshold depends on the field line co-latitude and on the black hole spin. The higher the spin, the easier the extraction. Globus & Levinson (2014) define the source term as a radial power law. In both publications, they find a low total energy extraction around the axis, which our results confirm. Pu et al. (2015) use a geometry obtained from a parabolic force free field solution. They inject pairs on a stagnation surface. They impose in addition two matching conditions at the stagnation surface, the continuity of Poynting flux and the equality of inflow and outflow pair fluxes. Their double flow

Solution	$\dot{J}_{\rm inj,open}$ (g.cm^2.s^{-1})	$\dot{J}_{\rm H,open}$ (g.cm^2.s^{-1})	$\dot{J}_{\rm H,tot}$ (g.cm^2.s^{-1})	$\dot{E}_{\rm inj,open}$ (erg.s^{-1})	$\dot{E}_{\rm H,open}$ (erg.s^{-1})	$\dot{E}^{\rm Poy}_{\rm H,open}$ (erg.s^{-1})	$\dot{E}_{\rm H,tot}$ (erg.s^{-1})	$\dot{E}^{\rm Poy}_{\rm H,tot}$ (erg.s^{-1})	$\dot{E}_{\rm out,open}$ (erg.s^{-1})
M1	$2,9\times10^{47}$	$1,4\times10^{47}$	6.4×10^{48}	5.9×10^{44}	-5.9×10^{44}	8.7×10^{41}	-3.6×10^{45}	3.2×10^{43}	1.3×10^{42}
M2	-2.7×10^{45}	3.4×10^{45}	5.6×10^{49}	6.2×10^{42}	-6.2×10^{42}	1.6×10^{39}	-3.4×10^{44}	1.2×10^{43}	1.1×10^{39}
M3	1.1×10^{47}	1.4×10^{47}	1.8×10^{48}	2.4×10^{43}	-2.2×10^{43}	3.7×10^{41}	-1.1×10^{44}	2.8×10^{43}	1.9×10^{42}

Table 5. Total angular momentum and power injected by pairs or extracted from the black hole for the three solutions in the region inside the last open field lines. $\dot{E}^{\rm Poy}_{\rm H,open}$ is the Poynting power extracted from the black hole inside the inner region. $\dot{J}_{\rm H,tot}$ $\dot{E}_{\rm H,tot}$ and $\dot{E}^{\rm Poy}_{\rm H,tot}$ are the angular momentum, the power and the Poynting power extracted from the whole black hole horizon. $\dot{E}_{\rm out,open}$ is the total power of the outflow spine jet in the inner region. .

solution is electromagnetically dominated and similar to the results of the GRMHD simulations of McKinney & Narayan (2007).

Several authors studied gaps in black hole magnetospheres (Levinson & Segev 2017; Hirotani & Pu 2016) showing that formation of a gap occurs for small accretion rate. In these works the multi-fluid flow geometry is fixed and mainly radial. The kinetic and the dynamics of the electron fluid, the positron one and the radiation are treated separately leading to a self-consistent model of pair formation. If the gap is spherical and the M87 black hole rotates maximally in Levinson & Segev (2017), we can estimate, with a maximal value of the magneto-spheric current in Fig.(2) of Levinson & Segev (2017), an amount of $\approx 10^{11}$g.s^{-1} for the pair mass rate produced inside the gap. This value is 7 order less than the rates we obtained in our solution, but pairs can also be created outside gaps. In fact, gaps are thought to be intermittent phenomena. They are locations where a small amount of created pairs is the reason for an intermittent emission at high energy.

Using an iterative procedure on the magnetic flux, the current and isorotation integrals, Nathanail & Contopoulos (2014) solve the Grad-Shafranov equation in a force free configuration. It allows, in the force free assumption, to recover the field geometry starting from a radial or a paraboloidal configuration. To pursue this theoretical approach, Huang et al. (2019) solve the Grad-Shafranov equation in the same way without neglecting the fluid forces, and simultaneously solve the Bernouilli equation. With different matching conditions compared to our model, they obtained double flow solutions with injection on the stagnation layer. Their 4-force $\mathbf{k}$ of the radiation field on the pair fluid is assumed to be equal to the product of the source term k_m and the 4-velocity $\mathbf{u}$. Huang et al. (2020) apply their model to produce double flow solutions for the stratified M87 jet. In their Cases V and VI, the outflow fluid energy is equal to 43% of the total energy, lower than the ratio we obtained for our M3 solution which is $\approx 71\%$.

Radiative GRMHD simulations (Crinquand et al. 2021 and Yao et al. 2021) have shown that the gap size is difficult to estimate and could be as small as $0.05r_g$. Moreover on the axis the gap could disappear as in the MAD W18 disk model of Yao et al. (2021). In this region, our solutions without a gap are very relevant to describe the double-flows near the polar axis. The value of electron temperature mention in Yao et al. (2021) is similar to ours. And the range of total amounts of created pairs is also close to the expected upper range.

5 CONCLUSIONS

We built three double-flow solutions from the meridional self-similar model presented in Chantry et al. (2018) respecting three minimal matching conditions for the model parameters in Eq.(58).

We have eight inflow parameters to fix and seven for the outflow. The three matching conditions reduce the number of free parameters in the outflow to four. In the future, we could limit these four degrees, first, to get the total current continuity condition, second, to obtain a smaller magnetosphere and to increase the horizon colatitude angle of the last opened field lines. We could also try to match the inflow with some radial solution for the outflow as the K4 solution presented in Chantry et al. (2018).

As expected the inflow acceleration is dominated by gravity. Pressure also plays a role, decelerating the inflow close to the stagnation layer and close to the black hole horizon and accelerating it in between. Due to the flaring geometry of the flux tube ($F < 0$) before the stagnation radius. The gravity works for opening the tubes where the radius increases, and is counter-balanced by the magnetic forces, mainly composed of magnetic poloidal pressure. For the transverse equilibrium, the pressure also counter-balances the gravity in the beginning and the end of the inflow.

The inflow model respects a scaling law similar to that mentioned in Zamaninasab et al. (2014) between the magnetic flux and the mass flux. Here, this scaling-law involves the inflow mass rate instead of the accretion mass rate and the efficiency is three times higher to create magnetic flux. One free inflow parameter has been fixed for that.

The discontinuity of the toroidal magnetic field and the line opening F across the stagnation surface lead to the existence of surface current and charge density on this surface.

This implies a contribution of the injected pairs to the electric current and then to the Poynting flux. This pair contribution to the Poynting flux has been calculated for the M3 solution and is comparable to the Poynting flux extracted from the black hole.

Inside the open field lines, the injected angular momentum at the stagnation surface could be of both signs and is of the same order of magnitude as the extracted one from the black hole. In terms of Noether's energy, most of the injected energy falls down into the black hole. Inside of the open magnetic field lines the energetic distribution is dominated by the inertial term. The black hole is fed by mass, kinetic and internal energy. Along the axis, the energetic budget is always dominated by the inertial energy (mass, gravitational, kinetic and internal energy). At larger colatitudes, the energetic budget is dominated by the inertial terms everywhere for I1, by the Lense-Thirring term for I2 and by the Poynting flux for I3. For the matching solution M3, the total Poynting power on the horizon, even if it is less than the inertial energy, represents a quarter of the total energy absorbed by the black hole.

Our solutions M2 and M3 require a large amount of injected mass but are located close to the upper boundary of our range of estimated mass injection rates by pair formation from hard disk photons. The M1 solution requires one order of magnitude more than the maximum mass injection rate. This means that in order to be valid M1 needs another mechanism of pair creation. The injection rate needed for M1 is likely to be unrealistic.

The use of meridional self-similar models to built inflow/outflow

leads to steady MHD solutions with some peculiarities, a high pair injection rate and a Poynting power in the inner region less than the matter energy power. All these peculiarities could be easily explained considering the fact this model is built to describe the MHD fields near the axis where the total power is matter dominated. Combining these models to describe fields near the axis with other semi-analytical models, more adapted to describe fields far from the axis, must be considered. As for the outflow, where the meridional self-similar model is used to describe spine-jet near the axis and radial self-similar model for the sheath layer or the disk wind. The inflow is probalby composed of different stratified components. In this scenario, which could be an improvement of the modelisation of black hole environment, the double spine jet energy principally comes from pair injection.

To conclude, the solution M3 is the most interesting solution, having an isorotation frequency equals to one half of the black hole one. It has a quite high but still reasonable injection mass rate and also a reasonable value for total outflow power. The final Lorentz factor of the outflow is around $\gamma \approx 10$. The extracted Poynting power from the black hole is comparable to the one given by a force-free model with the same isorotation value and the split monopole magnetic flux function of the same total magnetic flux. The Poynting power at stagnation surface of M3 outflow is a fourht of the ouflow power leading to a quite high magnetisation for meridional self-similar model solutions. The outflow power is inside the expected range for extragalactic jets.

REFERENCES

Bardeen J. M., Press W. H., Teukolsky S. A., 1972, ApJ, 178, 347
Beskin V. S., Par'ev V. I., 1993, Physics-Uspekhi, 36, 529
Beskin V. S., Istomin Y. N., Par'ev V. I., 1992, Soviet Ast., 36, 642
Blandford R. D., Znajek R. L., 1977, MNRAS, 179, 433
Camenzind M., 1986, A&A, 162, 32
Carter B., 2010, General Relativity and Gravitation, 42, 653
Ceccobello C., Cavecchi Y., Heemskerk M. H. M., Markoff S., Polko P., Meier D., 2018, MNRAS, 473, 4417
Chantry L., 2018, PhD thesis, PSL, ED127, Observatoire de Paris, http://www.theses.fr/2018PSLEO016/document
Chantry L., Cayatte V., Sauty C., Vlahakis N., Tsinganos K., 2018, A&A, 612, A63
Chantry L., Cayatte V., Sauty C., 2020, Classical and Quantum Gravity, 37, 105003
Chantry L., Dauvergne F., Temmam Y., Cayatte V., 2021, Classical and Quantum Gravity, 38, 145030
Chernikov N., 1963, Acta Physica Poloica, 24
Christodoulou D., 1970, Phys. Rev. Lett., 25, 1596
Crinquand B., Cerutti, B. Dubus, G. Parfrey, K. Philippov, A. 2021, A&A, 650, A163
Dadhich N., Tursunov A., Ahmedov B., Stuchlík Z., 2018, MNRAS,
Event Horizon Telescope Collaboration 2019, ApJ, 875, L1
Event Horizon Telescope Collaboration 2021, ApJ, 910, L13
Gebhardt K., Adams J., Richstone D., Lauer T. R., Faber S. M., Gültekin K., Murphy J., Tremaine S., 2011, ApJ, 729, 119
Ghisellini G., Tavecchio F., Chiaberge M., 2005, A&A, 432, 401
Globus N., Levinson A., 2013, Phys. Rev. D, 88, 084046
Globus N., Levinson A., 2014, ApJ, 796, 26
Globus N., Sauty C., Cayatte V., Celnikier L. M., 2014, Phys. Rev. D, 89, 124015
Gourgoulhon E., 2010, arXiv e-prints, p. arXiv:1003.5015
Gourgoulhon E., Jaramillo J. L., 2006, Physics Reports, 423, 159
Gourgoulhon E., Markakis C., Uryū K., Eriguchi Y., 2011, Phys. Rev. D, 83, 104007
Hirotani K., Okamoto I., 1998, ApJ, 497, 563
Hirotani K., Pu H.-Y., 2016, ApJ, 818, 50
Hirotani K., Takahashi M., Nitta S.-Y., Tomimatsu A., 1992, ApJ, 386, 455
Hirotani K., Pu H.-Y., Lin L. C.-C., Chang H.-K., Inoue M., Kong A. K. H., Matsushita S., Tam P.-H. T., 2016, ApJ, 833, 142
Huang L., Pan Z., Yu C., 2019, ApJ, 880, 93
Huang L., Pan Z., Yu C., 2020, ApJ, 894, 45
Kino M., Takahara F., Hada K., Doi A., 2014, The Astrophysical Journal, 786, 5
Koide S., Baba T., 2014, ApJ, 792, 88
Koide S., Shibata K., Kudoh T., Meier D. L., 2002, Science, 295, 1688
Komissarov S. S., 2004, MNRAS, 350, 1431
Komissarov S. S., 2005, MNRAS, 359, 801
Komissarov S. S., 2009, Journal of Korean Physical Society, 54, 2503
Komissarov S. S., McKinney J. C., 2007, MNRAS, 377, L49
Lasota J. P., Gourgoulhon E., Abramowicz M., Tchekhovskoy A., Narayan R., 2014, Phys. Rev. D, 89, 024041
Levinson A., Rieger F., 2011, The Astrophysical Journal, 730, 123
Levinson A., Segev N., 2017, Phys. Rev. D, 96, 123006
Marle C., 1969, Annales de l'I.H.P. Physique théorique, pp 67–126
Massaglia S., Bodo G., Rossi P., Capetti S., Mignone A., 2019, A&A, 621, A132
Mathews W. G., 1971, ApJ, 165, 147
McKinney J. C., 2006, MNRAS, 368, 1561
McKinney J. C., Narayan R., 2007, MNRAS, 375, 531
McKinney J. C., Tchekhovskoy A., Blandford R. D., 2012, MNRAS, 423, 3083
Meliani Z., Sauty C., Vlahakis N., Tsinganos K., Trussoni E., 2006, A&A, 447, 797
Nathanail A., Contopoulos I., 2014, ApJ, 788, 186
Nitta S.-y., Takahashi M., Tomimatsu A., 1991, Phys. Rev. D, 44, 2295
Penrose R., 1969, Nuovo Cimento Rivista Serie, 1
Penrose R., Floyd R. M., 1971, Nature Physical Science, 229, 177
Prieto M. A., FernÃ¡ndez-Ontiveros J. A., Markoff S., Espada D., GonzÃ¡lez-MartÃn O., 2016, Monthly Notices of the Royal Astronomical Society, 457, 3801
Pu H.-Y., Takahashi M., 2020, ApJ, 892, 37
Pu H.-Y., Nakamura M., Hirotani K., Mizuno Y., Wu K., Asada K., 2015, ApJ, 801, 56
Punsly B., Coroniti F. V., 1990, ApJ, 350, 518
Sauty C., Tsinganos K., 1994, A&A, 287, 893
Sol H., Pelletier G., Asseo E., 1989, MNRAS, 237, 411
Synge J., 1957, The Relativistic Gas. Series in physics, North-Holland Publishing Company, https://books.google.fr/books?id=HM1-AAAAIAAJ
Takahashi M., Nitta S., Tatematsu Y., Tomimatsu A., 1990, ApJ, 363, 206
Thorne K. S., 1987, The Membrane Paradigm for Black-Hole Astrophysics. Springer US, Boston, MA, pp 209–213, doi:10.1007/978-1-4613-1897-2_6, https://doi.org/10.1007/978-1-4613-1897-2_6
Toma K., Takahara F., 2016, Progress of Theoretical and Experimental Physics, 2016, 063E01
Vlahakis N., Königl A., 2003, ApJ, 596, 1080
Wagh S. M., Dadhich N., 1989, Phys. Rep., 183, 137
Wagh S. M., Dhurandhar S. V., Dadhich N., 1985, ApJ, 290, 12
Wald R. M., 1974, ApJ, 191, 231
Yao P. Z., Dexter J., Chen A. Y., Ryan B. R., Wong G. N., 2021, Monthly Notices of the Royal Astronomical Society, 507, 4864
Zamaninasab M., Clausen-Brown E., Savolainen T., Tchekhovskoy A., 2014, Nature, 510, 126
Znajek R. L., 1977, MNRAS, 179, 457

APPENDIX A: BEHAVIOUR OF THE INFLOW SOLUTIONS NEAR THE BLACK HOLE HORIZON

Let discuss how the model equations (see Annexe.(C) of Chantry et al. (2018)) and the four functions M^2, G^2, F, Π behave close to the black hole horizon. We adopt here all notations coming from Chantry et al. (2018). M is the Alfvén number on the polar axis, G the dimensionless cylindrical radius in unit of the Alfvén radius, F is the expansion factor of the streamlines and Π is the dimensionless pressure along the polar axis. The equations of the model are determined by the functions $\mathcal{D}, \mathcal{N}_{M^2}, \mathcal{N}_F$ and $\mathcal{N}_\Pi$ depending of R, M^2, G^2, F and Π. To determine the behaviour of our solutions near the black hole horizon, we need to express these functions at the radius $R = R_H = \frac{\mu}{2}\left(1+\sqrt{1-\left(\frac{2l}{\mu}\right)^2}\right)$ expressed in Alfvén radius unit). As explained in Chantry et al. (2018) and previous meridional self-similar models, we build from this model a constant, ϵ, which measures the efficiency of magnetic collimation (see Annexe.(C) of Chantry et al. 2018). This parameter writes,

$$\begin{aligned}\epsilon =& \frac{1}{h_z^2}\left[2\lambda^2\left(\frac{\Lambda^2 N_B}{D}+\frac{\bar{\omega}_z}{\lambda}\right)+\frac{\nu^2(2m_1-2e_1+\kappa-\delta)R}{(R^2+l^2)}\right.\\ &-\frac{M^4}{G^2h_\star^4(R^2+l^2)}\left(1-\frac{l^2}{(R^2+l^2)}+(\kappa-2m_1)\frac{(R^2+l^2)}{G^2}\right)\\ &\left.-\frac{\nu^2l^2RG^2}{(R^2+l^2)^3}+\frac{M^4h_z^2F^2}{h_\star^4G^2}\right]+\lambda^2\left(\frac{\Lambda N_V}{h_\star GD}\right)^2 . \end{aligned} \tag{A1}$$

Close to the black hole horizon, we have $h_z^2 \underset{R\to R_H}{\sim} \frac{2}{\mu}\frac{\sqrt{1-a^2}}{1+\sqrt{1-a^2}}(R-R_H)$. Numerically, we found that the function $h_zF \underset{R\to R_H}{\longrightarrow} 0$ near the horizon. The functions M^2 and G^2 remain finite and do not reach 0 on $R = R_H$. Since ϵ is constant, it implies that there exist a constant ϵ' such that,

$$\begin{aligned}&-\frac{M^4}{G^2h_\star^4(R^2+l^2)}\left(1+(\kappa-2m_1)\frac{X_+}{G^2}-\frac{l^2}{(R^2+l^2)}\right)-\frac{\nu^2l^2RG^2}{(R^2+l^2)^3}\\ &-\frac{\nu^2}{\mu}\left(2e^1-2m^1+\delta-\kappa\right)+2\lambda^2\left(\frac{\Lambda^2N_B}{D}+\frac{\bar{\omega}_z}{\lambda}\right)\underset{R\to R_H}{\sim}\epsilon' h_z^2 , \end{aligned} \tag{A2}$$

where we used $(R^2+l^2) = \mu R_H$ on the black hole horizon. The function $\mathcal{D}$ could have a singularity only for $R = 0$. The function $\mathcal{N}_{M^2}$ could also have a singularity if $G^2 = 0$ or $M^2 = 0$. Another possibility of singularity could happen for $R = R_H$. This function $\mathcal{N}_{M^2}$ can be rearranged as:

$$\begin{aligned}\mathcal{N}_{M^2} =& \frac{\mu h_\star^4 DRG^2}{2h_z^2X_+M^2}\frac{X_-}{X_+}\left[-\frac{M^4}{G^2h_\star^4}\left(1+(\kappa-2m_1)\frac{X_+}{G^2}-\frac{l^2}{X_+}\right)-\frac{\nu^2l^2G^2}{\mu^3R_H^2}\right.\\ &\left.-\frac{\nu^2}{\mu}\left(2e^1-2m^1+\delta-\kappa\right)+2\lambda^2\left(\frac{\Lambda^2N_B}{D}+\frac{\bar{\omega}_z}{\lambda}\right)\right]+R_{M^2} . \end{aligned}$$

R_{M^2} does not have any singularity for $R = R_H$. The equation Eq.(A2) insures the regularity of $\mathcal{N}_{M^2}\left(R, M^2, G^2, F, \Pi\right)$ when M^2, G^2, F, Π are solutions of model equations. It explains the numerical regularity of the M^2 function near the horizon. Indeed, we found numerically that M^2 reaches a limit value different of 0. Such arguments no longer hold for the F function. In this case, $\mathcal{N}_F\left(R, M^2, G^2, F, \Pi\right) \underset{R\to R_H}{\sim} \frac{\mathrm{Cst}}{h_z^2}$ (with a non vanishing constant), then we expect a behaviour such as $F \underset{R\to R_H}{\propto} \ln(R-R_H)$, which is the observed behaviour on the numerical solution. Nevertheless the angle of the magnetic field line with the radial direction χ is linked to the colatitude with,

$$\tan\chi = \frac{1}{2}\frac{\sqrt{X_+}h_zF}{R}\tan\theta . \tag{A3}$$

Then in Kerr metric, $\sqrt{X_+}h_zF/R$ is the significant geometrical quantity for the opening angle. This quantity reaches 0 on the horizon and the magnetic field lines enter radially in the horizon. The behaviour of F implies the convergence of G^2 to a finite value on the horizon.

The solutions of the model verify on the axis $\gamma\xi \underset{R\to R_H}{\longrightarrow} +\infty$ where ξ is the specific enthalpy. In order to avoid $\xi \underset{R\to R_H}{\longrightarrow} +\infty$, we could tune the inflow parameters to get $\gamma \underset{R\to R_H}{\sim} 1/h_z$ on the horizon. This requirement also induces the Π function behaviour on the horizon. It implies that $\nu^2h_\star^4 - \frac{\mu M^4}{G^4} \underset{R\to R_H}{\sim} h_z^2$ and using the model equations, we get $\Pi \underset{R\to R_H}{\propto} \ln(R-R_H)$ behaviour on the horizon instead of $\Pi \underset{R\to R_H}{\propto} (R-R_H)^{-1}$ without this requirement. Nevertheless, this requirement is difficult to obtain pratically during the matching procedure between inflow and outflow solutions.

APPENDIX B: INTEGRATION OF CONSERVATIONS LAW

The key of direct integration of Eq.(33,34), is the use of lenght of flux tube from the black-hole horizon ℓ in poloidal submanifold. This lenght could be define as an improper integrals which converge as easily intuite using an isometric embedding (Chantry et al. 2021). Nevertheless,

following methods of Lasota et al. (2014) integration of Noether current conservation could gives additional information and especially the horizon boundary condition.

B1 Integration of Noether current conservation

From both definition of Noether current Eqs.(25,26), definition of Killing vector and conservation of motion equation $\nabla \cdot \mathbf{T}_{\rm MHD} = \mathbf{k}$ we get,

$$\nabla \cdot \mathbf{P}_{\rm MHD} = -\mathbf{k} \cdot \boldsymbol{\eta} \,,$$

where ∇ is four dimensional usual covariant derivative. Instead of using 3+1 plus stationnary and axisymetry assumption as it is done to get Eqs.(31,32), let follow Lasota et al. (2014) and use Stokes' theorem on the integrals of previous equation on an arbitrary space-time volume element $\mathcal{U} \subset \mathcal{M}$. This imply,

$$\int\limits_{\partial\mathcal{U}} \boldsymbol{\epsilon}\left(\mathbf{P}_{\rm MHD}, \mathbf{dy}^1, \mathbf{dy}^2, \mathbf{dy}^3\right) = -\int\limits_{\mathcal{U}} \mathbf{k} \cdot \boldsymbol{\eta} \sqrt{-g} d^4x \,, \tag{B1}$$

(B2)

where ϵ is the ordinary Levi-Civita tensor. $\mathbf{dy}^1, \mathbf{dy}^2, \mathbf{dy}^3$ must be three linearly independent quadri-vector infinitesimal vector on $\partial\mathcal{U}$, such that, if $\mathbf{O}$ is a quadrivector directed outward $\mathcal{U}$, $(\mathbf{O}, \mathbf{dy}^1, \mathbf{dy}^2, \mathbf{dy}^3)$ is direct base of tengeant space (i.e. $\epsilon(\mathbf{O}, \mathbf{dy}^1, \mathbf{dy}^2, \mathbf{dy}^3) > 0$).

Choose a space time volume adapted to our problem help us to give more information on the field on black hole horizon.

B2 4D flux tube and frontier geometry

In the following, for a given value of magnetic flux $A \in [0, A_H[$, a given value of boyer lindquist radius $r \in]r_H, +\infty[$ and a given value of Boyer-Lindquist time coordinate t we will note,

$$\mathcal{T}^t_{A,r} = \{M \in \Sigma_t \,|\, A(M) = A \,, r_H \leq r(M) \leq r\} \,,$$

a given flux tube embed in the Σ_t foil, cut under a given radius and for a given time. For two given magnetic flux $A_1 < A_2$ and a time intervals $t_1 < t_2$ we will note,

$$\mathcal{U}^{t_1,t_2}_{A_1,A_2,r} = \bigcup_{\substack{t_1 \leq t \leq t_2 \\ A_1 \leq A \leq A_2}} \mathcal{T}^t_{A,r} \,,$$

the space-time volume construct by union of flux tube between two time foil and two flux tube. Because we will calculate flux integrals on the border of $\mathcal{U}^{t_1,t_2}_{A_1,A_2,r}$ it will be helpful to gives information on its border $\partial\mathcal{U}^{t_1,t_2}_{A_1,A_2,r}$,

$$\mathcal{V}^{t_1}_{A_1,A_2,r} \bigcup \mathcal{V}^{t_2}_{A_1,A_2,r} \bigcup \mathcal{B}^{t_1,t_2}_{A_1,r} \bigcup \mathcal{B}^{t_1,t_2}_{A_2,r} \bigcup \Delta\mathcal{H}^{t_1,t_2}_{A_1,A_2} \bigcup \mathcal{S}^{t_1,t_2}_{A_1,A_2,r} \,,$$

where $\mathcal{V}^{t_1}_{A_1,A_2,r}$ ($\mathcal{V}^{t_2}_{A_1,A_2,r}$) is inter flux tube on a space foil Σ_{t_1} (Σ_{t_2}),

$$\mathcal{V}^{t}_{A_1,A_2,r} = \bigcup_{A_1 \leq A \leq A_2} \mathcal{T}^t_{A,r} \,,$$

$\mathcal{B}^{t_1,t_2}_{A_1,r}$ ($\mathcal{B}^{t_1,t_2}_{A_2,r}$) is the union of interior (exterior) flux tube for the considered time intervals,

$$\mathcal{B}^{t_1,t_2}_{A,r} = \bigcup_{t_1 \leq t \leq t_2} \mathcal{T}^t_{A,r} \,,$$

$\Delta\mathcal{H}^{t_1,t_2}_{A_1,A_2}$ is the part of the horizon for $t_1 \leq t \leq t_2$ where the flux tube $A_1 \leq A \leq A_2$ are anchored,

$$\Delta\mathcal{H}^{t_1,t_2}_{A,r} = \{M \in \mathcal{H} \,|\, A_1 \leq A(M) \leq A_2 \,, t_1 \leq t \leq t_2\} \,,$$

and finally $\mathcal{S}^{t_1,t_2}_{A_1,A_2,r}$ the union on time intervals of exterior spherical corona,

$$\mathcal{S}^{t_1,t_2}_{A_1,A_2,r} = \{M \in \mathcal{M} \,|\, r(M) = r \,, A_1 \leq A(M) \leq A_2 \,, t_1 \leq t \leq t_2\} \,. \tag{B3}$$

Apply the result Eq.(B1) apply on this volumes and specific border require to specify adapted $\mathbf{dy}^1, \mathbf{dy}^2, \mathbf{dy}^3$ for each of these hypersurface.

B2.1 Inter flux tube on a space foil

It is the easiest one, because it is a spatial hypersurface, the normal directed toward the exterior is $+\mathbf{n}$ for $\mathcal{V}^{t_2}_{A_1,A_2,r}$ ($-\mathbf{n}$ for $\mathcal{V}^{t_1}_{A_1,A_2,r}$). Embedded in Σ_t we could choose,

$$\mathbf{dy}^1 = h_r dr \mathbf{e}_r \,, \; \mathbf{dy}^2 = h_\theta d\theta \mathbf{e}_\theta \,, \; \mathbf{dy}^3 = h_\varphi d\varphi \mathbf{e}_\varphi \,.$$

Thus, if we note,

$$E^t_{A_1,A_2,r} = \int\limits_{\mathcal{V}^t_{A_1,A_2,r}} \mathbf{T}_{\rm MHD}(\mathbf{n},\boldsymbol{\eta}) h_r h_\theta h_\varphi dr d\theta d\varphi$$

the contribution of the two inter flux tube to the integrals in the left hand side of Eq.(B1) is,

$E^{t_2}_{A_1,A_2,r} - E^{t_1}_{A_1,A_2,r}$

which is the difference of Noether energy inside of the inter flux tube between two time. Stationary assumption imply it is equals to 0 in our case.

B2.2 Union of flux tube for the time intervals

$\mathcal{B}^{t_1,t_2}_{A,r}$ is a timelike hypersurface since $\boldsymbol{\nabla} A$ is normal to it and is spacelike quadrivector. By construction this set could be rewrote,

$$\mathcal{B}^{t_1,t_2}_{A,r} = \{M \in \Sigma_t \mid A(M) = A\,, r_H \leq r(M) \leq r\,, t_1 \leq t \leq t_2\}\,,$$

since, because A is time independent, $dt\boldsymbol{\eta}$ is tangent to this set. With the notation $\mathbf{e} = \mathbf{B}_p/||\mathbf{B}_p||$ which is tangent to the set we could complete the infinitesimal base,

$\mathbf{dy}^1 = h_\varphi d\varphi \mathbf{e}_\varphi$, $\mathbf{dy}^2 = cdt\boldsymbol{\eta}$, $\mathbf{dy}^3 = d\ell\mathbf{e}$.

Nevertheless, the equations Eqs.(28) imply that $\mathbf{P}_{\rm MHD}$ is also tangent to the set. And then,

$$\epsilon\left(\mathbf{P}_{\rm MHD}, \mathbf{dy}^1, \mathbf{dy}^2, \mathbf{dy}^3\right) = 0$$

and consequently, its contribution is 0.

B2.3 Union on time intervals of exterior spherical corona

It is also a timelike surface since $\mathbf{e}_r$ is a spacelike quadri-vector normal and directed outward to $\mathcal{S}^{t_1,t_2}_{A_1,A_2,r}$. Its definition Eq.(B3) allow to choose,

$\mathbf{dy}^1 = h_\theta d\theta \mathbf{e}_\theta$, $\mathbf{dy}^2 = h_\varphi d\varphi \mathbf{e}_\varphi$, $\mathbf{dy}^3 = cdt\boldsymbol{\eta}$.

Then after few line of calculation, this contribution to the left hand side of Eq.(B1) is,

$$E^{t_1,t_2,\rm ext}_{A_1,A_2} = \int\limits_{\theta_1}^{\theta_2} \frac{\Psi_A \mathcal{E}}{2} \partial_\theta A d\theta\,(t_2 - t_1) = \int\limits_{A_1}^{A_2} \frac{\Psi_A \mathcal{E}}{2} dA\,(t_2 - t_1) \tag{B4}$$

B2.4 Part of the horizon

As it is well know and explain by Carter (2010) as a consequance of ridity theorem the horizon is a null hypersurface. Following, Lasota et al. (2014) we introduce the quadrivector,

$$\ell = \boldsymbol{\eta} + \frac{\Omega}{c}\boldsymbol{\xi}$$

is a null vector, which is normal to $\mathcal{H}$. As a null normal, $\boldsymbol{\eta}$ is also tangent to $\mathcal{H}$. Let introduce $\mathcal{S}_t = \mathcal{H} \cap \Sigma_t$ a temporal section of the horizon. It is possible to construct a null quadri-vector $\boldsymbol{\kappa}$, orthogonal to $\mathcal{S}_t$ and whith $\boldsymbol{\kappa} \cdot \boldsymbol{\ell} = -1$. Find more details on construction of $\boldsymbol{\ell}$ and $\boldsymbol{\kappa}$ on Gourgoulhon & Jaramillo (2006). The null base $(\boldsymbol{\kappa}, \boldsymbol{\ell}, \mathbf{e}_\theta, \mathbf{e}_\varphi)$ is direct. Furthermore, because $\boldsymbol{\kappa}$ and $\boldsymbol{\ell}$ are orthogonal to $\mathbf{e}_\theta$ or $\mathbf{e}_\varphi$) and also because $-\left(\boldsymbol{\epsilon}(\boldsymbol{\kappa}, \boldsymbol{\ell}, \mathbf{e}_\theta, \mathbf{e}_\varphi)\right)$ is equals to the determinant of the Gram matrice of these vector we get,

$$-|\boldsymbol{\epsilon}(\boldsymbol{\kappa}, \boldsymbol{\ell}, \mathbf{e}_\theta, \mathbf{e}_\varphi)|^2 = \det \mathrm{Gram}(\boldsymbol{\kappa}, \boldsymbol{\ell}, \mathbf{e}_\theta, \mathbf{e}_\varphi) = \begin{vmatrix} 0 & -1 & 0 & 0 \\ -1 & 0 & 0 & 0 \\ 0 & 0 & 1 & 0 \\ 0 & 0 & 0 & 1 \end{vmatrix} = -1$$

and then $\boldsymbol{\epsilon}(\boldsymbol{\kappa}, \boldsymbol{\ell}, \mathbf{e}_\theta, \mathbf{e}_\varphi) = 1$.

Because $\boldsymbol{\kappa}$ is directed inward, we choose,

$\mathbf{dy}^1 = cdt\boldsymbol{\ell}$, $\mathbf{dy}^2 = h_\theta d\theta \mathbf{e}_\theta$, $\mathbf{dy}^3 = h_\varphi d\varphi \mathbf{e}_\varphi$.

Using the usual null decomposition,

$$\mathbf{P}_{\rm MHD} = -c(\mathbf{P}\cdot\boldsymbol{\ell})\boldsymbol{\kappa} - (\mathbf{P}\cdot\boldsymbol{\kappa})\boldsymbol{\ell} + \mathbf{P}_{\mathcal{S}_t}\,,$$

leads to a contribution of the left hand side of Eq.(B1),

$$\Delta E^{t_1,t_2,\mathcal{H}}_{A_1,A_2} = 2\pi c \int\limits_{\theta_1}^{\theta_2} \mathbf{T}_{\rm MHD}(\boldsymbol{\ell}, \boldsymbol{\eta}) h_\theta \varpi d\theta (t_2 - t_1)\,. \tag{B5}$$

B2.5 Reduce the space time volum

Firstly, choose infinitesimaly close flux tube $A_1 = A$ and $A_2 = A + dA$, we get,

$$\left[\frac{\Psi_A \mathcal{E}}{2}\partial_\theta A d\theta + 2\pi c \mathbf{T}_{\rm MHD}(\boldsymbol{\ell},\boldsymbol{\eta}) h_\theta \varpi d\theta\right](t_2 - t_1) = -\int_{\mathcal{U}} \mathbf{k}\cdot\boldsymbol{\eta}\sqrt{-g}d^4x$$

where we note $\mathcal{U}^{t_1,t_2}_{A_1,A_2,r} = \mathcal{U}$ to reduce the amount of notation.

Secondly, we take the limit $r \longrightarrow r_H$, the right hand side of previous equation vanish. Then we got,

$$\lim_{r\to r_H} \frac{\Psi_A \mathcal{E}}{2}\partial_\theta A + 2\pi c \mathbf{T}_{\rm MHD}(\boldsymbol{\ell},\boldsymbol{\eta}) h_\theta \varpi = 0 \tag{B6}$$

B3 Horizon boundary condition

B3.1 Boundary conditions from previous work

Usual covariant scalar field as ρ_0 must remain smooth at horizon radius. In the following we will also consider that all scalar quantities derived from 3+1 ideal, stationnary and axisymetric MHD, more explicitely A, Ω, Ψ_A, L and $\mathcal{E}$ needs to be smooth at horizon radius. It could be deduce from the covariant derivation of these quantity (see Gourgoulhon et al. (2011)). It also imply the regularity of xh and $x_{\rm RM}$ involve in the relation of constant inversion (see Eq.(32,33,34) of Chantry et al. (2018)). From all of this and expression of $\mathbf{B}_p$ we deduce that $\mathbf{B}_p$ is smooth and also that $B^\theta = O(h)$ at horizon. Relation $4\pi\rho\gamma h\mathbf{V}_p = \Psi_A \mathbf{B}_p$ imply that $\gamma h V_p$ is also smooth. Because V_p must be limited by c it imply regularity of $h\gamma$ we deduce $\gamma = O(1/h)$. We also get $V^\theta = O(h)$. Inversion of constant of motion (see Eq.(32,33,34) of Chantry et al. (2018)) we deduce that $V^{\hat\varphi} = O(h)$, $B^{\hat\varphi} = O(1/h)$ and $\xi = O(1)$. Thus we deduce from previous result that we must have $1 - {\beta^{\hat r}}^2 = O(h^2)$ and then because the flow must enter in the horizon,

$$1 + \frac{V^{\hat r}}{c} = O(h^2) \tag{B7}$$

From smooth character of A and Ω and the expression of electric field Eq.(23) we have,

$$E^{\hat r} = O(h) \quad \text{and} \quad E^{\hat\theta} = O(1/h) \tag{B8}$$

B3.2 The boundary condition

Let calcul the quantity involve in Eq.(B6) for fluid component. We get, after few line of calculation,

$$2\pi h_\theta \varpi \rho \xi c^2 \left[(h\gamma)^2\left(1 + \frac{V^{\hat r}}{c}\right)\left(1 + \frac{\varpi\omega V^{\hat\varphi}}{hc^2}\right) - \frac{Ph^2}{\rho_0 \xi c^2}\right],$$

which is then a $O(h^2)$ and reach 0 whithout bring any additionnal constraint. It is more interesting for the electromagnetic field. First, remind that,

$$T^{\rm EM}_{\alpha\beta} = \frac{1}{4\pi}\left[F_{\mu\alpha}F^{\mu}{}_{\beta} - \frac{F_{\mu\nu}F^{\mu\nu}}{4} g_{\alpha\beta}\right]$$

It induce after few line of calculation, that the electromagnetic contribution to the quantity involve in the limit Eq.(B6) is,

$$-ch_\theta\varpi\left[\left(hE^{\hat\theta} + hB^{\hat\varphi}\right)\left(\frac{3\Omega - \omega}{2c}\partial_\theta A + \frac{hB^{\hat\varphi}}{2}\right) + h^2\left(\frac{B_p^2}{2} + \frac{\Omega E^{\hat r}\Sigma}{c\rho^2}\partial_r A\right)\right]$$

which reach 0 if,

$$\lim_{r\to r_H}\left(hE^{\hat\theta} + hB^{\hat\varphi}\right) = 0 \tag{B9}$$

APPENDIX C: GRADIENT DESCENT TECHNIQUES

To adapt the input parameter of the outflow to the inflow instead of using a simple technique of optimisation of a residual function, we decide to follow the direction in parameter space obtain by a look like Gram-Schmidt orthogonalisation of gradient of our quantity in term of parameter. Indeed, the minimisation of a residual function often leads to difficulties of different kinds. Sometimes this leads us to regions of the parameter space whose solutions are non-physical, regions where the automation of the crossing of the slow magnetosonic point undergoes a discontinuity due to the non-linearity of the equations or is impossible, or something else. Then, we need to explore the parameter space using different possibility for the chosen direction.

	λ	κ	δ	ν	μ	e_1	a	$\Omega/\omega_{\mathcal{H}}$	γ_∞	$R_{\rm sta}/R_{\mathcal{H}}$
S1	1.171	0.291	1.319	0.600	0.184	-0.063	0.519	0.502	10.04	1.175
S2	1.170	0.286	1.325	0.613	0.187	-0.049	0.519	0.502	10.03	1.225
S3	1.169	0.280	1.333	0.627	0.190	-0.037	0.519	0.502	10.05	1.275
S4	1.169	0.274	1.336	0.641	0.193	-0.027	0.519	0.502	10.05	1.325
S5	1.170	0.269	1.341	0.655	0.196	-0.016	0.519	0.502	10.04	1.375
S6	1.173	0.265	1.345	0.668	0.198	-0.004	0.519	0.502	10.09	1.425
S7	1.177	0.260	1.349	0.681	0.200	0.009	0.519	0.502	10.05	1.475
S8	1.182	0.257	1.353	0.694	0.202	0.022	0.519	0.502	10.08	1.525

Table C1. Set of parameters for 8 solutions calculated in order to get different values of stationary radius, keep constant the final Lorentz factor, isorotation and spin of the black hole.

Be more explicit, for the matching, we need to find the outflow parameter $(\lambda, \kappa, \mu, \nu, l, \mu, e_1)$ such the quantities,

$$\begin{aligned} f_1 &= \frac{R_{\rm sta}}{\mu} \\ f_2 &= \frac{l}{\mu} \\ f_3 &= \frac{\mu^3}{2\left(1+l^2\right)^2} + \frac{\lambda\mu^{3/2}}{\nu}\sqrt{1-\frac{\mu}{1+l^2}} \end{aligned} .$$

are equals to some specific values (the corresponding inflow value Eq.(58)). In what follow, we discuss a more general procedure where we have n (with $n \leq 7$) function $(f_k)_{k=1,...n}$ of the solution parameter $(\lambda, \kappa, \mu, \nu, l, \mu, e_1)$ to adapt. We will refer to them as control function.

If we note,

$$u_k = \nabla f_k \in \mathbb{R}^7 \quad \text{for} \quad k \in [\![1, n]\!] .$$

Suppose $(u_k)_{k=1,...n}$ are linearly dependent, and call E_n the subspace generated by linear combinaison of $(u_k)_{k=1,...n}$ and $E_{n,j} = \text{Span}\{u_k \mid k = 1...n \text{ and } k \neq j\}$ for each $j = 1...n$. Then,

$$\exists! d_j \in E_n \text{ such that } \begin{cases} ||d_j|| = 1 \\ d_j \cdot u_j > 0 \\ d_j \perp E_{n,j} \end{cases} ,$$

d_j is the normalised orthogonal to $E_{n,j}$ projection of u_j. We calculate d_j using recurrence formula. Let note $p_n\left(u_j; (u_k)_{\substack{k=1...n \\ k\neq j}}\right)$ the unit vector embed in E_n, orthogonal to $E_{n,j}$ and such that $d_j \cdot u_j > 0$. Then forall $i \neq j$ it follow that,

$$p_n\left(u_j; (u_k)_{\substack{k=1...n \\ k\neq j}}\right) = p_{n-1}\left(p_2(u_j; u_i); (p_2(u_k, u_i))_{\substack{k=1...n \\ k\neq j \\ k\neq i}}\right) \tag{C1}$$

which allow to explicitly calculate d_j considering that for each non-colinear vector u, v,

$$p_2(u; v) = \frac{u - \dfrac{u\cdot v}{||v||^2} v}{\left\| u - \dfrac{u\cdot v}{||v||^2} v \right\|} . \tag{C2}$$

If we note $s = (\lambda, \kappa, \mu, \nu, l, \mu, e_1)$, then for all j and for a small displacement εd_j we expect that for all $i \in [\![1, n]\!]$ a typical behaviour,

$$f_i(s + \varepsilon d_j) = f_i(s) + \delta_{ij}\varepsilon\left(u_i \cdot d_j\right) + O(\varepsilon^2) .$$

which makes it possible to deal with the control functions one after the other. Nevertheless due to the strong non-linear behaviour of the system of equation mention in the appendix of Chantry et al. (2018), the control function could suffer of a lot of discontinuity, which imply the local character of this method. More the family $(u_k)_{k=1,...n}$ is close to orthogonal family, more this method is efficient.

Practically we estimate the gradient by a second order estimation of the partial derivative. We put in the Tab.(C1) the result obtain using such a method. We choose for control function the spîn a, the isorotation $\Omega/\omega_{\mathcal{H}}$, the final Lorentz factor γ_∞ and the stagnation radius $R_{\rm sta}/R_{\mathcal{H}}$. Then we follow the direction such the evolution of spin, isorotation and final Lorentz is at order two therefore evolution of stagnation radius is positive and order 1. This method can be used to fit the solutions of the southern self-similar model to the observational constraint.

This paper has been typeset from a TEX/LATEX file prepared by the author.